APPLICATION OF SCANNING CORRELATION SPECTROSCOPY TECHNIQUES TO QUANTIFY DNA DOUBLE STRAND BREAK REPAIR KINETICS IN THE LIVING CELL AFTER EXPOSURE TO γ-RAYS AND RADIOMIMETIC CHEMICALS

by

SALIM ABDISALAAM

Presented to the Faculty of the Graduate School of
The University of Texas at Arlington in Partial Fulfillment
of the Requirements
for the Degree of

DOCTOR OF PHILOSOPHY

THE UNIVERSITY OF TEXAS AT ARLINGTON
August 2012

ACKNOWLEDGEMENTS

First, I would like to thank my advisor and mentor, Dr. George Alexandrakis for his constant advice and encouragement to strive to do good research. He is been very resourceful in almost all field of science, someone you will always want to be in your team.

. I would like to thank my committee members Dr. Matthew Petroll, Dr. Digant Dave and Dr. Baohong Yuan for their guidance and their time. And special thanks to Dr. David Chen who has been supporting our research tremendously and gave us the opportunity to work in his lab with open arms. I would also like to thanks Dr. Chaitanya Nirodi for his guidance and support in EGFR experiments.

Also, I would like to thanks my lab members in biomedical engineering department and all lab members in molecular radiation oncology lab for their support and help me in different ways.

.

ABSTRACT

APPLICATION OF SCANNING CORRELATION SPECTROSCOPY TECHNIQUES TO QUANTIFY DNA DOUBLE STRAND BREAK REPAIR KINETICS IN THE LIVING CELL AFTER EXPOSURE TO γ-RAYS AND RADIOMIMETIC CHEMICALS

Salim Abdisalaam, PhD

The University of Texas at Arlington, 2012

Supervising Professor: George Alexandrakis

The kinetics of most proteins involved in DNA damage sensing, signaling and repair following ionizing radiation exposure cannot be quantified by current live cell fluorescence microscopy methods. This is because most of these proteins, with only few notable exceptions, do not attach in large numbers at DNA damage sites to form easily detectable foci in microscopy images. As a result a high fluorescence background from freely moving and immobile fluorescent proteins in the nucleus masks the aggregation of proteins at sparse DNA damage sites. Currently, the kinetics of these repair proteins are studied by laser-induced damage and Fluorescence Recovery After Photobleaching (FRAP) that rely on the detectability of high fluorescence intensity spots of clustered DNA damage. However, the traditional laser-induced hot-spot accumulation and FRAP methods are not applicable for studying the repair of sparse damage created by γ-irradiation or radiomimetic chemicals, which are more relevant agents of cancer treatment than laser-induced clustered damage. Firstly, the use of Fluorescence Correlation Spectroscopy (FCS), a long-standing technique for quantifying the concentration, diffusion coefficient and the binding kinetics of fluorescently tagged proteins was considered for its usability to address the challenge of quantifying sparse damage kinetics. As part of this effort, initial work focused on establishing FCS capability on test systems with spatial uniformity of protein kinetics as these were known to be amenable to analysis by FCS, before this method was applied to the new area of DNA repair kinetics. The test systems chosen were aqueous solutions of purified DNA repair proteins mixed with short double stranded DNA fragments and an endothelial growth factor receptor (EGFR) live cell system in which EGFR translocated from the cell membrane to the nucleus after γ-irradiation. Though application of FCS to these systems proved successful, when FCS was subsequently applied to the quantification of sparse damage repair kinetics in the living cell it was found that this method yielded high variability in the determined concentrations and effective diffusion coefficients of DNA repair proteins in the nucleus, which was attributed to spatial heterogeneity of the bound fraction and to bleaching artifacts resulting from the protracted point illumination that FCS requires. Subsequently, scanning correlation spectroscopy techniques known as Number and Brightness (N&B) and Raster Image Correlation Spectroscopy (RICS) were applied to the sparse damage kinetics problem as these latter methods involved spatial averaging of kinetics over a user-selected area of the cell with reduced photobleaching, which held promise for reducing the variability of results. Two key double strand break repair proteins, namely Ku 70/80 and the DNA-dependent protein kinase catalytic subunit (DNA-PK$_{CS}$), were employed as specific examples to showcase the feasibility of using N&B and RICS, results of this work indicated that these methods were suitable to use for quantification of the repair kinetics of sparse DNA damage, which was not currently attainable in DNA repair studies to date. Importantly, these methods could be used to quantify the kinetics of other DNA damage sensing, signaling, and repair proteins in the living cell and could thus contribute towards improving our understanding of the mechanisms controlling cancer treatment response.

TABLE OF CONTENTS

APPENDIX

LIST OF ILLUSTRATIONS

LIST OF TABLES

Table Page

CHAPTER 1

INTRODUCTION

The kinetics of most proteins involved in DNA damage sensing, signaling and repair following ionizing radiation or radiomimetic agent exposure cannot be quantified by current live cell fluorescence microscopy methods. This is because most of these proteins, with only few notable exceptions [1, 2], do not attach in large numbers at DNA damage sites to form easily detectable foci in microscopy images. As a result a high fluorescence background from freely moving and immobile fluorescent proteins in the nucleus masks the aggregation of proteins at sparse DNA damage sites. Currently, the kinetics of these repair proteins are studied by laser-induced damage and Fluorescence Recovery After Photobleaching (FRAP) that rely on the detectability of high fluorescence intensity spots of clustered DNA damage [3-5]. However, laser-induced damage is complicated in nature and each type of DNA damage is repaired by different pathways [6]. For example, base cross-linking damage is recognized and processed by the nucleotide-excision repair (NER) pathway; base damage caused by abnormal nucleotide modification by the base-excision repair (BER) pathway; and DNA double-strand breaks (DSBs) by non-homologous end-joining (NHEJ), homologous recombination (HR), or single-strand annealing (SSA) pathways [6]. Dissecting the kinetics of different DNA repair pathways requires the creation of a single type of DNA damage at a time. The focus of this work is the study of DSBs as these are considered the most cytotoxic of DNA lesions, primarily repaired by the NHEJ pathway, and if misrepaired may lead to chromosomal translocations and genomic instability that can then lead to cancer [7]. We create DSBs in different cell lines by exposure to γ-rays or a radiomimetic chemical called bleomycin, which are DSB-forming agents [7, 8]. In this work it is shown that significant differences in DNA repair protein kinetics exist for sparse DNA damage created by γ-rays or bleomycin versus the kinetics of laser-induced clustered damage in the cell nucleus. Therefore laser-induced damage may not always be a physiologically relevant surrogate for understanding repair mechanisms activated by sparse DNA damage created by treatment methods that are more relevant to cancer therapy.

Motivated by these comparisons with laser-induced damage kinetics in this work the feasibility of applying Raster Image Correlation Spectroscopy (RICS) and Number and Brightness (N&B) analysis protocols for live cell imaging [9, 10] was investigated as a novel means of enabling the monitoring of changes in kinetics of fluorescently tagged repair proteins during sparse DSB damage conditions. RICS measures molecular diffusion coefficients and concentration of fluorescently tagged proteins [9]. N&B measures concentration and effective molecular brightness of fluorescently tagged proteins, which increases with protein agglomeration [10]. A measured decrease in free protein concentration, a decrease in apparent diffusion coefficients due to binding-unbinding, or an increase in apparent agglomeration are all quantitative measures to assess DNA repair response as a function of time after DNA damage. We study the kinetics of two key DSB repair proteins, namely the Ku 70/80 heterodimer and the DNA-dependent protein kinase catalytic subunit (DNA-PKcs) [3], as specific examples to showcase the feasibility of the proposed methods to quantify kinetics for DNA repair proteins after sparse damage. Ku70/80 has a ring-like structure that enables it to thread through the broken DSB ends and act as the DNA break recognition molecule that then recruits DNA-PKcs as one of the key proteins regulating the formation of molecular complexes that process and repair the DSBs [11]. DNA-PK is a member of the phosphatidylinositol-3-kinase (PI-3-K)-related kinase (PIKK) super family, other member in this family includes the human ataxia telangiectasia mutated (ATM) and ATM-Rad3 related (ATR) proteins [12-14]. To validate that the RICS and N&B analysis results are consistent with the current understanding of DSB repair biology, DNA-PKcs repair kinetics are quantified for the wild type (WT) and repair-deficient (7A) forms in which all 7 major phosphorylation sites (Thr2609-Thr2647 and Ser2056) are replaced with alanine residues, the latter being phosphorylation-deficient and expected to disengage more slowly from

DSBs compared to WT. Furthermore, Wortmannin, a general PI3k inhibitor that inhibits DNA-PKcs kinase activity [15], is used as an additional control to demonstrate that Ku70/80 residence times at DSBs are also increased if DNA-PKcs disengagement is inhibited.

The central hypothesis of this work is that the RICS and N&B methods can be used to quantify the kinetics of DSB repair proteins in live cells after sparse DNA damage. To our knowledge RICS and N&B have so far been explored very little [16] as a potentially transformative technology for the DNA repair field and we are the first group to have studied ionizing radiation induced DNA repair kinetics in living cells [17]. The traditional hot-spot accumulation and FRAP methods [3] are not applicable to sparse damage, and the only other long-standing technique that may help with that is Fluorescence Correlation Spectroscopy (FCS) [18]. FCS measures the diffusion coefficient and concentration of fluorescently tagged proteins, as does RICS, but in FCS measurements are spatially confined to the size of a single confocal volume [18]. One perceived difficulty with FCS is that, because it is a point-and-shoot technique, it would be impossible to know where DNA damage occurred in the nucleus so as to point at that spot. However, the change in protein bound fraction, and therefore of the free fraction, is global as repair proteins bind-unbind and diffuse around the nucleus making this response measurable by FCS. However, we found that FCS yielded high variability in the determined concentration and diffusion coefficient of proteins in the nucleus that we attribute to spatial heterogeneity of the bound fraction and to bleaching artifacts resulting from protracted point illumination, as discussed below. In contrast, the RICS and N&B methods are raster scanning techniques that incur less photobleaching and yield protein kinetics that are the average over a user-selected region of interest (ROI) that can be as large as the entire nucleus[9], thus yielding less variable results [9, 19]. FCS, RICS and N&B measurements were all performed using a confocal system equipped with a photon counting detector attachment as shown in Fig. 1.1. In this work, after some preliminary studies validating the use of FCS in an aqueous solution system of interacting repair proteins with DNA fragments, comparison between scanning versus point correlation spectroscopy methods was performed in an endothelial growth factor receptor (EGFR) live cell system (chapter 3), known to be amenable to study by FCS [20], to verify that RICS and N&B approaches yield more consistent results relative to FCS. Subsequently, the RICS and N&B methods were applied to the quantification of DNA repair protein kinetics.

Even though the results presented in this study only pertain to DNA-PKcs and Ku70/80, the methods presented here are potential applicable to a broader number of DNA repair proteins participating in the HR and NHEJ pathways. Therefore application of RICS and N&B analysis to the DNA repair field opens up many possibilities for studying repair pathways in a setting that mimics cancer radiation therapy and chemotherapy.

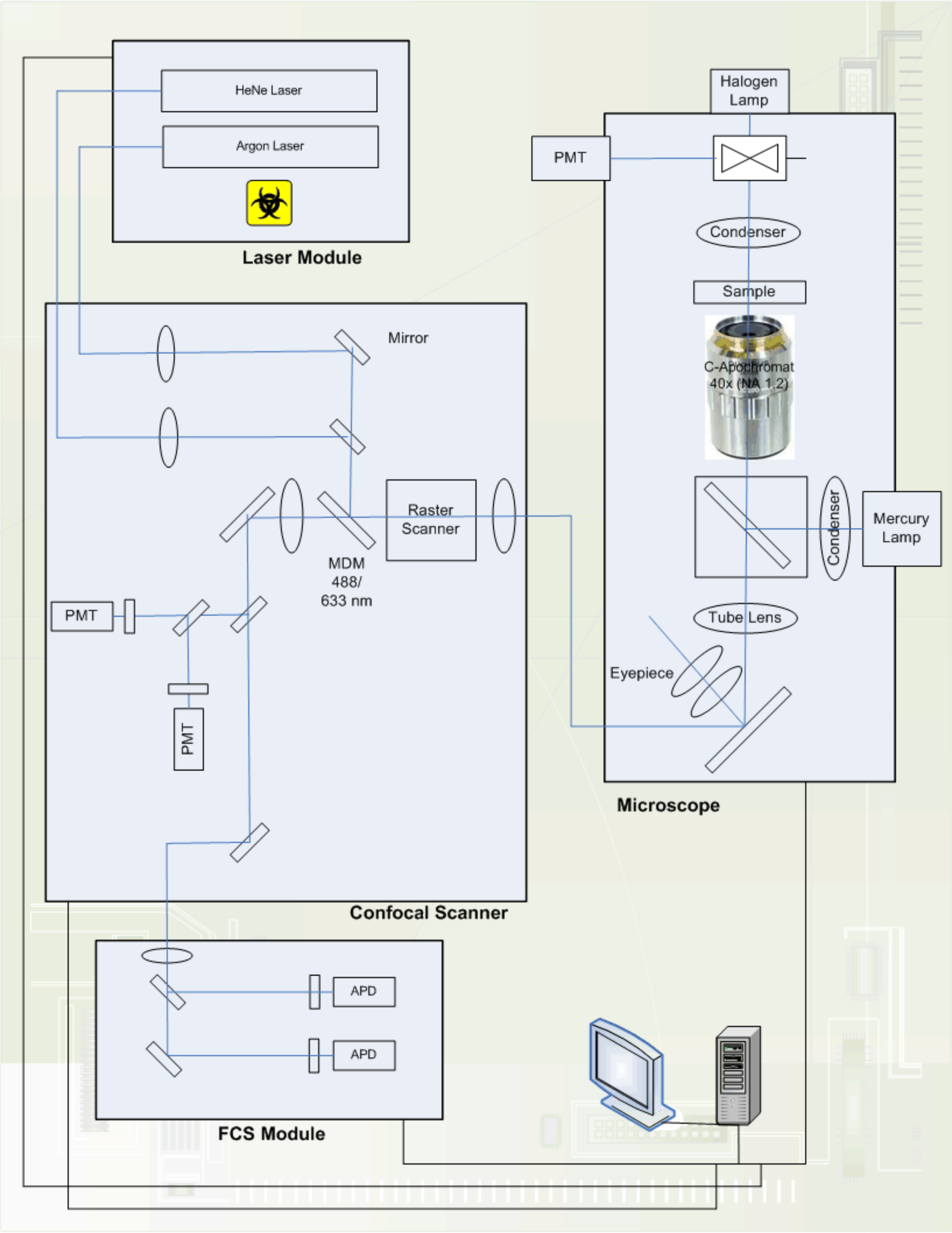

Figure 1.1 Typical confocal imaging system.

CHAPTER 2

BACKGROUND

2.1 Laser induced damage and time-lapse imaging to quantify protein recruitment kinetics

In order to study recruitment kinetics in live cells for nonhomologous end-joining proteins; time lapse imaging method has been used extensively. This imaging technique has been used to study recruitment of DNA-PKcs [22], Ku80 [23], ATM [24, 25] and 53bp1. In this method a 365-nm pulsed nitrogen laser (Spectra-Physics, Mountain View, CA, USA) is directly coupled to the epifluorescence path of the microscope (Fig. 2.1) in order to be used to induce DSBs in a specified ROI of the cell nucleus [22, 26]. Using this method, it has been shown that the fluorescently tagged protein accumulates at DSB sites, forming a visible hot spot that reaches maximum accumulation at ~10-15 minutes post-damage [26]. Subsequently, as the DSB repair progresses, these proteins dissociate and the hot spot intensity reduces accordingly. Usually the kinetics of wild type proteins are monitored and compared to kinetics of mutant variants in order to observe any differences in accumulation kinetics between the two. Protein kinetics at DNA DBSs are usually monitored up to 2 hrs post-damage, but sometimes longer time points are employed, up to 24 hrs.

Recruitment kinetics measurements are done using confocal laser scanning microscopy which entails the raster scanning of sample by galvo-driven mirrors. After the laser beam has been reflected by the scanning mirrors, it passes through a dichroic mirror and then through the objective lens and into the sample. The red-shifted fluorescence emission is separated from the excitation light at the dichroic mirror (since the wavelength is higher) and then reaches the detector, which can be a photomultiplier tube (PMT) or an avalanche photodiode (APD) as shown in figure 2.1.

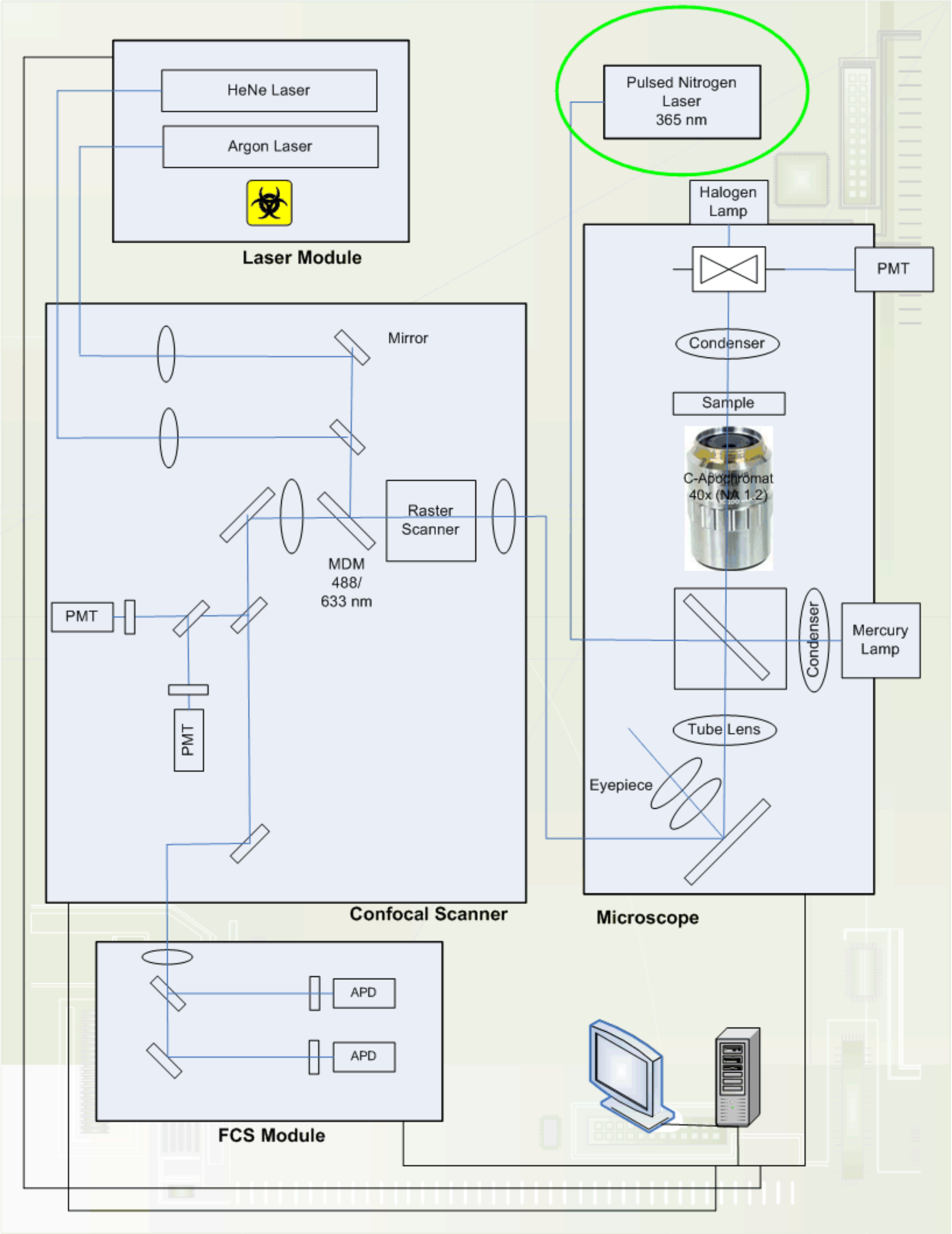

Figure 2.1 Confocal system (same as figure 1.1) with nitrogen pulse laser attachment for FRAP measurements [21].

2.2 FRAP as applied in DNA repair kinetics

FRAP has been used to study recovery rate of different NHEJ proteins including DNA-PKcs [22], Ku70/80 [12, 23], ATM [24, 25], 53bp1, XLF [26], XRCC4[26] and Artemis [12] and more generally, it has been used to study the dynamics of fluorescent proteins in vivo since almost 40 years ago [27]. FRAP measurements are usually performed with a confocal microscope system that is equipped with appropriate hardware to control the exposure intensity and accurate timing of such measurements. For DNA repair kinetics studies, a hot spot of repair protein is first created with a 365 nm nitrogen laser (Fig. 2.1) and then FRAP is applied onto that hot spot. Fluorescence intensities of nuclear regions away from the hot spot are also measured to calculate the net fluorescence intensity of the accumulated protein at the damage sites. Then, the change in relative fluorescence intensity (*RF*) with time (*t*) is given by:

$$RF(t) = \frac{\left(I(t) - I_{pre}\right)}{(I_{\max} - I_{pre})} \qquad (2.0)$$

where $I(t)$ is the average fluorescence of the photobleached accumulation spot that is normalized to the pre-bleach accumulation intensity, I_{max}, and I_{pre} is the pre-bleach intensity [22]. FRAP measurements are performed by photobleaching the entire protein accumulation spot that formed after maximum accumulation of DSBs proteins at the damage site, which typically occurs 10-15 min post-damage. Photobleaching is immediately followed by measurements of fluorescence recovery that are attained by imaging the entire chosen FOV rapidly and in contiguous time intervals. The ROI over which the recovered fluorescence is integrated is usually circular in shape to match the accumulation of proteins in the damage site. Images are taken in every 10-30 seconds for up to 10 minutes, depending on how quickly proteins disengage from the damage sites [22]. These FRAP measurements are also intensity corrected for unintended bleaching during repetitive imaging of the same FOV during fluorescence recovery. The resulting kinetics are typically interpreted qualitatively though sometimes they are fit to putative kinetic models [28, 29].

2.3 Fluorescence correlation spectroscopy (FCS)

FCS has been a useful technique to study single molecule interactions for several decades [30-33]. In the early days of FCS these measurements were faced with poor signal-to-noise ratio, but incorporation of confocal microscopy reduced the noise from the background and increased the sensitivity to a high level [34]. FCS (Fig. 2.2) extracts information from a sample due to transits of fluorescently tagged molecules in thermodynamic equilibrium at low concentration, so that fluctuations of the occupancy of the focal volume create fluctuations in detected fluorescence intensity, which is the basis of the FCS signal [35]. The fluorescence intensity fluctuations $\delta I(t)$, resulting from the diffusing fluorescent molecules in confocal volume, when correlated with fluorescence intensity fluctuations after time $(t + \tau)$ yield the normalized intensity autocorrelation function $G(\tau)$:

$$G(\tau) = 1 + \frac{< \delta I(t) \delta I(t + \tau) >}{< I >^2} \tag{2.1}$$

where the brackets describe the time average and $<I>$ the mean fluorescence intensity [36-38]. The autocorrelation function due to the Brownian motion of the protein molecules in a 3-D Gaussian volume element with half axes 'ω_{xy}' and 'ω_z' is described as

$$G(\tau) = 1/N\left(1 + \frac{\tau}{\tau_D}\right)^{-1}\left(1 + \left(\omega_{xy}/\omega_z\right)^2 \frac{\tau}{\tau_D}\right)^{-1/2} \tag{2.2}$$

Here, ω_{xy} denotes the $1/e^2$ radial radius of Gaussian confocal volume, and ω_z is the axial radius of the confocal volume.

$$\tau_D = \omega_{xy}^{\ 2}/(4D) \tag{2.3}$$

τ_D being the diffusion time and *D* the diffusion coefficient [37, 39]. The average number of molecules, *N*, in the confocal volume is given by

$$N = CV_{eff} \tag{2.4}$$

where V_{eff} is the effective confocal volume [40] given by

$$V_{eff} = \pi^{3/2} S\omega_{xy}{}^{3} \tag{2.5}$$

where *S* is the structure parameter [40] given by

$$S = \omega_z / \omega_{xy} \tag{2.6}$$

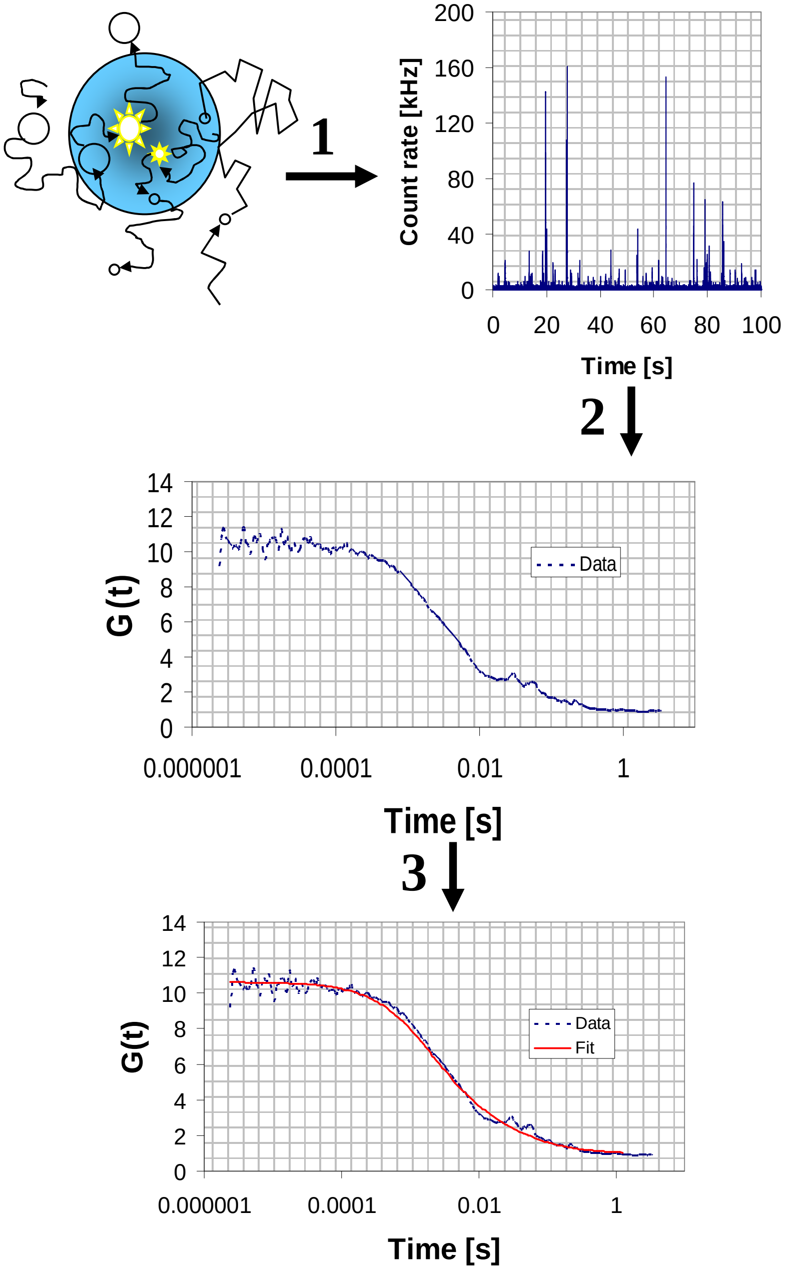

Figure 2.2 Main principles steps of FCS: (1) Measuring intensity fluctuation (2) Calculating correlation function (3) Fitting to a biophysical model [21, 32].

2.4 Raster-scan Image correlation spectroscopy (RICS)

FCS is a very dependable method to monitor kinetics of proteins in homogeneous solutions in *vitro*, but is challenging to apply *in vivo*. FCS is particularly challenged by photobleaching especially if it is applied to the monitoring of molecules with slow kinetics, e.g. large diffusing complexes or molecules that are binding-unbinding to immobile structures, especially if multiple time-course measurements are required [41]. The RICS and N&B methods are raster scanning techniques that therefore incur less photobleaching [9, 19]. RICS is an extension of the Image Correlation Spectroscopy (ICS) technique [42], and is related to other scanning techniques that are based on ICS, such as, temporal-ICS (TICS), spatiotemporal-ICS (STICS), k-space ICS (kICS) [43].

The correlation image of the RICS data can be calculated using Eq. 2.7 [9, 44].

$$G_{RICS}(\xi,\psi) = \frac{\langle I(x,y)I(x+\xi,y+\psi)\rangle}{\langle I(x,y)\rangle^2} \tag{2.7}$$

where the angle bracket indicates average spatial locations in both *x* and *y* directions, and where ξ and ψ are the spatial increments in the *x* and *y* directions, respectively [44, 45]. The data obtained from this correlation image can then be fitted using Eq. 2.8 [9, 44].

$$G(\xi,\psi) = G_D(\xi,\psi) * G_S(\xi,\psi) * G_T(\xi,\psi) \tag{2.8}$$

Eq. 2.8 has three components, one due to correlation between neighboring pixel intensity values due to particle diffusion, G_D (Eq. 2.9), one due to correlation between neighboring pixel intensity values due to beam raster scanning, G_S (Eq. 2.10) and finally a correlation due to blinking as a result of triplet state excitation, G_T (Eq. 2.11) where τ_p is the pixel dwell time in x, τ_l is the interline time in y [9, 44, 46]

$$G_D(\xi,\psi)=\gamma/N\left(1+\frac{4D(\tau_p\xi+\tau_l\psi)}{w_{xy}{}^2}\right)^{-1}\left(1+\frac{4D(\tau_p\xi+\tau_l\psi)}{w_z{}^2}\right)^{-1/2} \qquad (2.9)$$

$$G_S(\xi,\psi)=\exp\left(-\frac{\left(\frac{\delta r}{w_{xy}}\right)^2(\xi^2+\psi^2)}{1+\frac{4D(\tau_p\xi+\tau_l\psi)}{w_{xy}{}^2}}\right) \qquad (2.10)$$

$$G_T(\xi,\psi)=1+Ae^{-(\tau_p\xi+\tau_l\psi)/\tau} \qquad (2.11)$$

Stacks of images for RICS analysis are acquired using a laser scanning microscope. The set scan speed depends on the molecular weight of the protein [45]. First the cell to be measured is selected and a stack of images is acquired (50 to 100 images). The electronic zoom of the microscope is selected to have a high enough value so that neighboring pixels are overlapping, a necessary condition for RICS measurements [44, 45]. The zoom decides the FOV size and an ROI within that FOV is then selected, different numbers of pixels can be used usually 256 x 256. A region of interest, usually a clip box of 128 x 128 pixels (Fig 2.3), is acquired from an image of 256 x 256 pixels during data analysis in order to compute the 2D spatial correlation [9, 43, 44]. In this work the computed correlation function was fit to a model of diffusion dynamics [9]. Other dynamics such as binding can be obtained by correlation analysis by using different fitting models [44]. For the RICS experiments the selection of pixel size and scan speed are critical to measuring spatio-temporal correlations successfully [44, 45]. It is important to avoid both over-sampling and under-sampling while taking RICS measurements (Fig 2.4). Scanning parameters values for both objectives used in this project (C-Apochromat 40x/1.2 W corr and Plan-Apochromat 63x/ 1.4 Oil Ph3) have been shown in appendix B. Also, appendix B shows guidelines of valid scanning parameter range in order to try to avoid both over-sampling and under-sampling of pixels while scanning images.

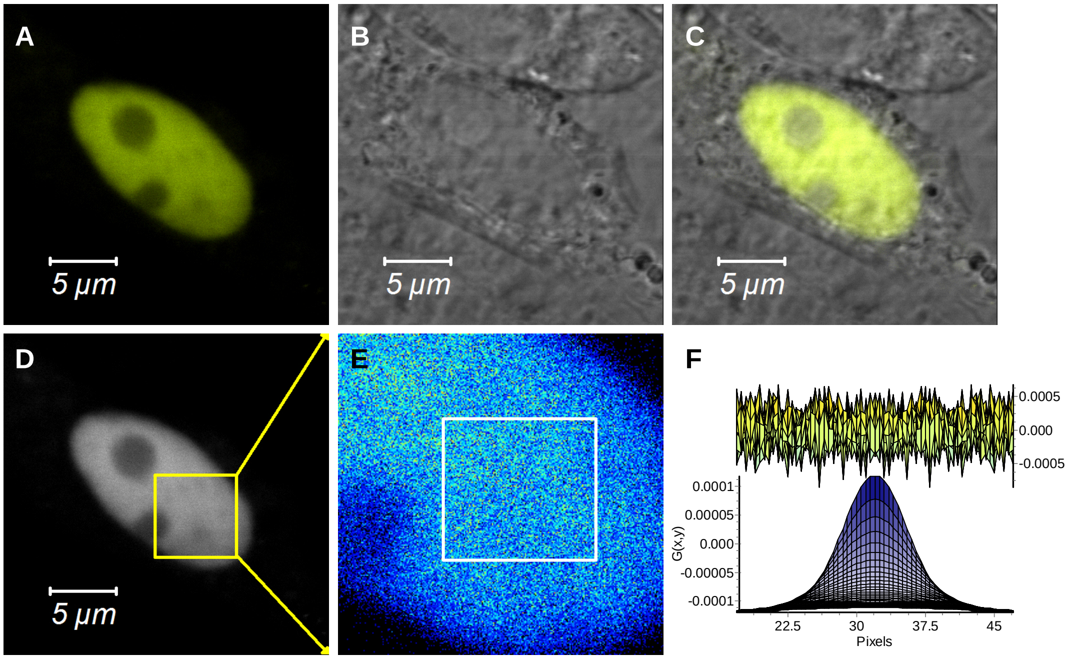

Figure 2.3 (A) Confocal image of an Xrs6 cell expressing GFP-Ku80; (B) DIC image of A (C) Merge of confocal and DIC images (D) Selected region of the nucleus to be included in RICS analysis; (E) Snapshot of the fluorescence intensity fluctuations in a background-corrected image of the selected region of interest; (F) Fitting of the 2D correlation curve.

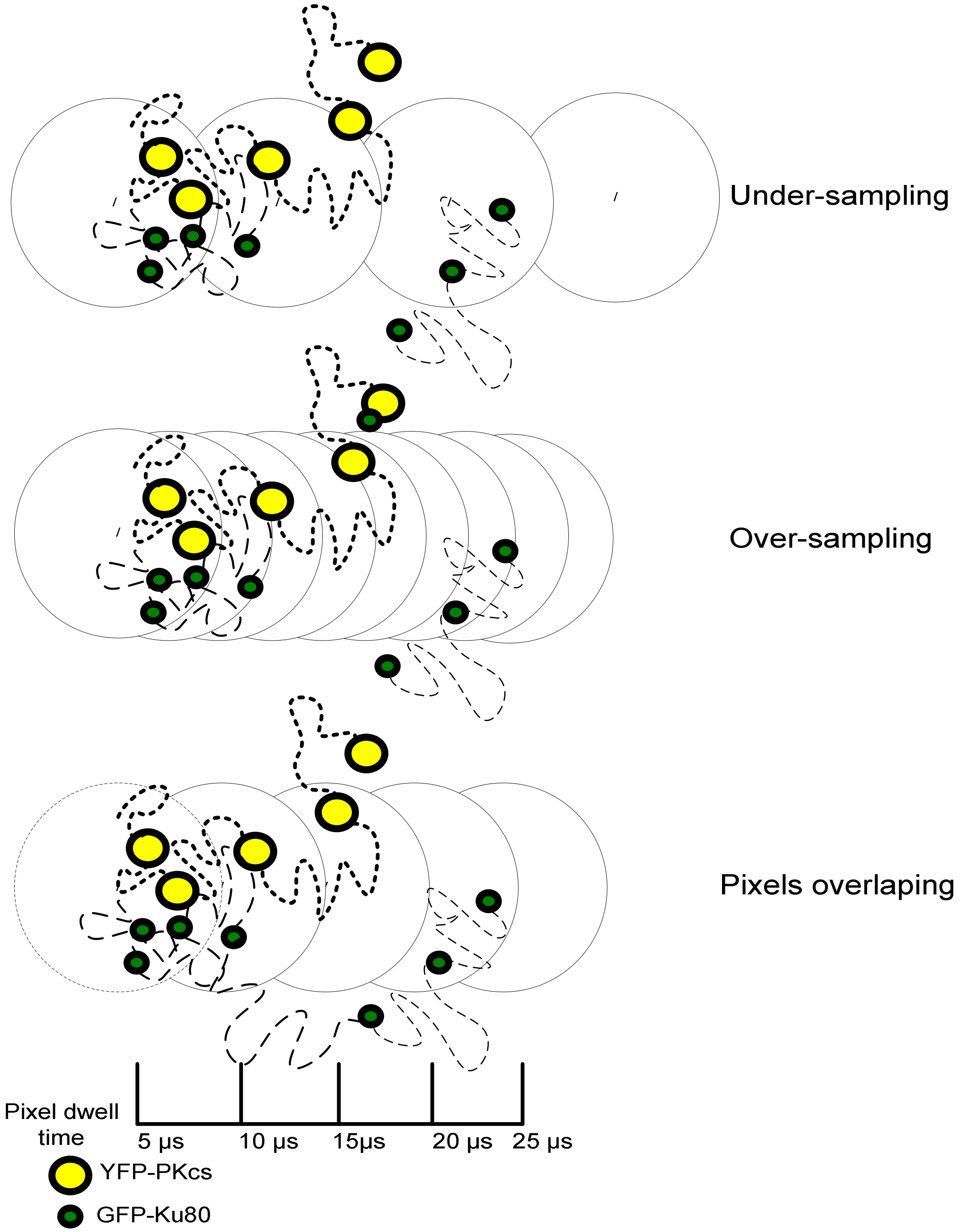

Figure 2.4 Pixels sampling: Lower panel shows pixels should overlap for good correlation, middle panel shows pixels over-sampling and upper panel shows pixels under-sampling.

2.5 Number and Brightness (N&B) analysis

N&B analysis is based on the detection of time-series fluorescence signals, obtained at regular time intervals, equal to the time the beam takes to return to the same pixel as an image is raster scanned repetitively. N&B analysis gives information about the effective molecular concentration and the agglomeration status of fluorescently tagged proteins [45, 47, 48]. In a given pixel obtained from the raster scan image, the apparent brightness *(B)* and apparent number of molecules *(N)* (Figure 2.4) are related to variance (σ^2) and average intensity ($<k>$) as shown in Eqs. 2.12 and 2.13 below [19, 48]:

$$B = \frac{<k>}{<N>} = \frac{\sigma^2}{<k>} \tag{2.12}$$

$$N = \frac{<k>^2}{\sigma^2} \tag{2.13}$$

However, these B and N values contain signal fluctuation contributions both due to molecular mobility as well as due to detector shot noise and the immobile molecule background. The background-corrected quantities indicating the actual number of molecules n and molecular brightness ε are given by the following equations [45, 47]:

$$n = \frac{<k>^2}{\sigma^2 - <k>} \tag{2.14}$$

$$\varepsilon = \frac{\sigma^2 - <k>}{<k>} \tag{2.15}$$

CHAPTER 3

QUANTIFY WT-EGFR KINETICS AND ITS TWO MUTANT VARIANTS IN THE CELL MEMBRANE AND IN THE NUCLEUS BEFORE AND AFTER γ- IRRADIATION USING FCS, RICS AND N&B ANALYSIS.

3.1 Introduction

The epidermal growth factor receptor (EGFR) is one of the ErbB family member of receptor tyrosine kinases (RTK) [49, 50]. ErbB family members include ErbB1 (EGFR), ErbB2, ErbB3 and ErbB4 [51, 52]. EGFR is a trans-membrane protein which is activated following binding with either EGF-ligand or tumor necrosis factor (TNF)-alpha [53, 54]. When the EGF family ligand binds EGFR or other ErbB family member receptors it induces the formation of either homo- or hetero-dimers [55, 56], which in turn undergo intermolecular tyrosine phosphorylation. The phosphorylated dimers then initiate several intracellular signaling cascades that play an important role in cell survival, cell proliferation and cell migration [57, 58]. EGFR is over-expressed in most epithelial cancer cells, in some cases up to 100 times more than the normal EGFR population. Over-expressed EGFR triggers uncontrollable cancerous cell proliferation.

Radiation therapy is a common cancer treatment modality. When cells are exposed to ionizing radiation (IR) the ensuing formation of reactive oxygen species (ROS) that react with DNA cause DNA damage [59]. EGFR is thought to be implicated in the reduction of radiosensitivity of cancer cells by activating a key DNA repair protein named DNA-PKcs through a pathway that is not as yet fully understood [60-62]. Understanding the mobility and interaction kinetics of EGFR with its ligands and translocation to the nucleus is crucial for studying its implication in decreasing radiosensitivity. Fluorescence Correlation Spectroscopy

(FCS) has been used to study this receptor's mobility and kinetics in living cells for over a decade [20, 63]. In FCS, the fluctuations of fluorescently tagged molecules passing through a micron-size confocal detection volume are used to quantify the underlying kinetic parameters such as molecular concentration, and diffusion coefficients or binding constants [64]. When FCS measurements are performed in living cells these kinetic parameters may have high variability due to spatial heterogeneity of the bound fraction of fluorescently tagged molecules and to bleaching artifacts resulting from protracted point illumination. In contrast, scanning correlation techniques proposed in recent years, namely Number and Brightness (N&B) analysis [47, 65] and Raster-Scan Image Correlation Spectroscopy (RICS) [44, 45] have been shown to be advantageous for living cell measurements because these are performed over a user-selected region of interest (ROI), which results in less photobleaching and better spatial averaging of potential measurement heterogeneities.

In this study, N&B analysis has been employed to demonstrate the nuclear translocation of EGFR and its mutants from the cell membrane to the nucleus of living cells after γ-irradiation alone, or in combination with an EGFR-blocking antibody (cetuximab) treatment. These experiments were done in order to further corroborate prior immunofluorescence measurements that WT-EGFR plays a radioprotective role by translocating to the nucleus and interacting with DNA-PKcs [50, 66], while EGFR mutants do not translocate to the nucleus. Also, in order to study the effect of mutant EGFR on the translocation of WT-EGFR to the nucleus, transient transfections of EGFP-EGFR (WT) in stable HBEC cells with different Ds-Red EGFR backgrounds (WT, L858R and ΔE746-E750) were performed, followed by N&B measurements of the EGFP-EGFR component as a function of time post-irradiation. Figure 3.1 summarizes the existing model of nuclear translocation kinetics for WT-EGFR and mutant-EGFR after γ-irradiation and cetuximab treatment [50].

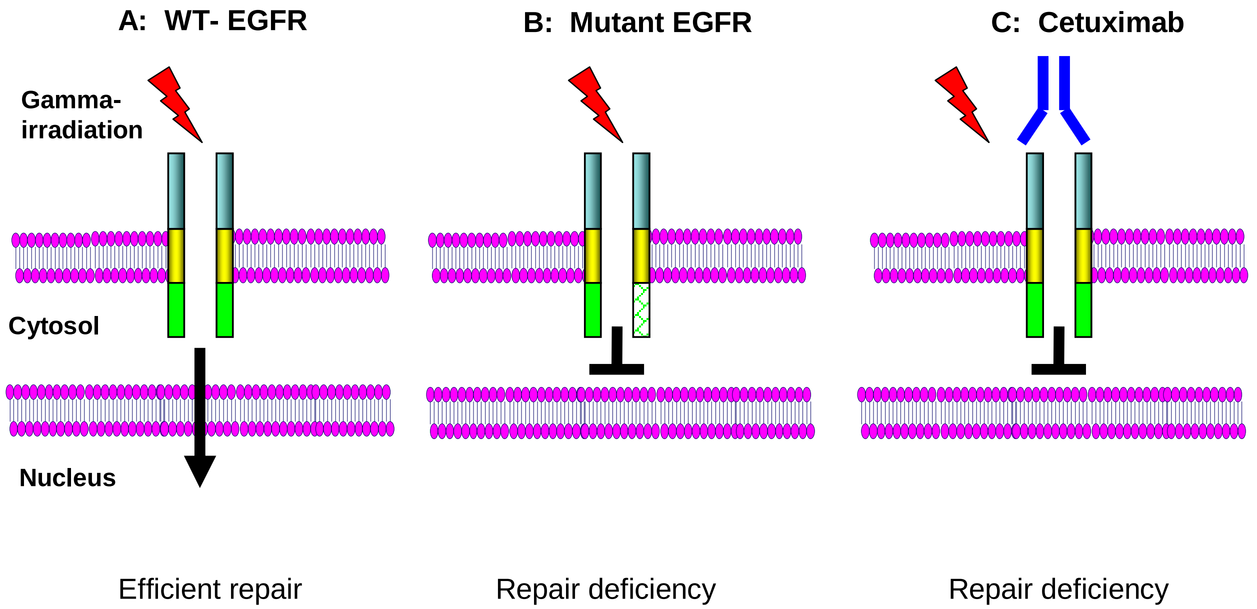

Figure 3.1: Existing nuclear translocation model for WT-EGFR and its mutants: (A) WT-EGFR translocates to the nucleus after ionizing radiation, (B) Mutant forms of EGFR exert a radiosensitizing effect by associating with the wild-type EGFR and blocking its nuclear import and interactions with DNA-PKcs. (C) Concurrent treatment with cetuximab augments radiosensitizing effect through a blockade of WT-EGFR nuclear translocation [50].

3.2 Materials and Methods

3.2.1 Cell culture and γ-irradiation

Human bronchial epithelial cells (HBEC) were maintained in Keratinocyte cell culture medium (Invitrogen), supplemented with 4 µg/µl Blasticidin, 10 µg/µl Geneticin, 250 ng/µl Puromycin, 1% penicillin, 0.2 ng/ml recombinant human EGF and 30 µg/ml bovine pituitary extract. All cells were maintained in 5 % humidified CO_2 incubator at 37^oC. For transient transfection experiments, cells were grown to 50% confluency and then transfected with 2 µg (per 35-mm dish) of DNA (EGFP-wtEGFR) along with 200 µl of jetPrime Buffer and 4 ul of jetPrime reagent from Polyplus-Transfection (Illkirch, France). Transfection reagents were added to 2 ml of Keratinocyte (free of antibiotics) medium in 35-mm tissue culture dishes (Greiner bio-one). Cells were divided 14-18 hours after transfection and grown in 35-mm glass-bottom dishes (MatTek Cultureware) and measurements were taken 24 hr following cell splitting, with confluency of ~60%. During the measurements cells were maintained in CO_2-independent medium (Invitrogen) at 37℃. Before eac h experiment, cells were irradiated with 4 Gy of γ-irradiation using a ^{137}Cs irradiator (Mark 1 irradiator, JL Shepherd & Associates).

3.2.2 N&B method setup for EGFR kinetics measurements

Confocal images for N&B analysis [67] were acquired using an LSM 510 Meta (Carl Zeiss MicroImaging GmbH, Jena) equipped with avalanche photodiodes that were part of ConfoCor3 attachment (Version 4.2,Carl Zeiss MicroImaging GmbH, Jena, Germany). A 40x water immersion C-Apochormat objective lens with N.A of 1.2 was used. The scan speed was set at 12.8 µs/pixel which corresponded to 1.96 seconds per frame and 50 frames were collected for each measurement. The scan area was selected to be away from the edges of the cell nucleus and was 256 x 256 pixels. A region of interest, a clip box of 128 X 128 pixels, was cropped from an image of 256 x 256 pixels during data analysis. The electronic zoom of the microscope was set to 15 in order to attain the necessary spatial sampling conditions for N&B measurements [67] , which resulted in a field of view of to 9.52 µm x 9.52 µm. In order to test the accuracy of the system to recover a known number of particles, fluorescent bead experiments were performed. For the green channel, green fluorescent beads (Duke Scientific) were used and for the red channel, red fluorescent beads (Duke Scientific) were used. Beads of both fluorescence colors had a 25 nm diameter.

For EGFP-EGFR HBEC cells, measurements were obtained using a 488 nm argon laser with 4 µW of excitation power at the focal spot. A dichroic mirror (HFT 488/543) was used to route laser excitation power onto the sample. To exclude any excitation light leakage, a band pass filter (BA 505–540 IR) was used before the detector. For DsR-EGFR HBEC cells, a 543 nm HeNe laser was used at an excitation power of 3 µW at the focal spot. Detection of fluorescence was performed using a dichroic mirror (HFT 488/543) and a band pass filter (BA 580–610 IR) in front of the detector. Cells were selected such that expression levels produced concentration values in the tens of nM range, The position of these cells was then marked using the available Zeiss microscope software (LSM 510, version 4.2). Stacks of 50 images were acquired for each marked cell prior to γ-irradiation and then the cells were irradiated with 4 Gy in the irradiator room and immediately brought back in the nearby microscopy room. Subsequently, the same cells were located and measured in time sequence for up to one hour after irradiation. The first measurement was acquired 5 minutes after irradiation, and then measurements were acquired at approximately 20, 40 and 60 minutes post-irradiation for each cell. Ten cells were used for each time point measured. The resulting image stacks were analyzed by N&B analysis software, which is commercially available (Globals, Laboratory for Fluorescence Dynamics, Irvine, CA). The output of N&B analysis gives the number of molecules and average brightness per pixel in the acquired images. From the bead calibration studies the size of the confocal detection volume was obtained and this number was used to calculate the concentration of EGFR molecules from the deduced number of molecules per pixel. All experimental time point results were expressed as percentage change of EGFR molecule concentration inside the nucleus with respect to the value attained after 5 minutes of irradiation.

Results were not normalized to a time-point pre-irradiation because a loss of fluorescence intensity was noticed immediately after irradiation. As a result the normalization point was selected to be the first available one after irradiation. The time it took to bring the cells back from irradiator room to the microscopy room and find the same cells was about 5 min. The duration of irradiation was approximately 1 minute and 6 seconds. Using these methods we quantified the post-irradiation kinetics for WT EGFR and two mutants (L858R and ΔE746-E750) in the cell nucleus. The percentage changes in the concentration of EGFR molecules were quantified for each type of EGFR. The statistical significance of any differences between these EGFR receptor type concentrations, across the ensemble of time-points where measurements were performed, was tested by linear mixed model analysis [68].

3.3 Results and Discussion

3.3.1 Effect of γ-irradiation on the nuclear translocation of wild type and mutant EGFR in HBEC cells

No significant change was observed in the translocation of EGFR in stable HBEC mutants L858R (n=10) and ΔE746-E750 (n=10) transfectants in the nucleus up to one hour after 4-Gy γ-irradiation (Fig. 3.2). On the other hand there was considerable increase in nuclear EGFR concentration for stable HBEC WT cells (n=10), reaching ~ 80% after one hour of irradiation (55 minutes after the first measurement). Mixed linear model analysis [68] indicated a statistically significant percent change in EGFR concentration between WT and L858R ($p<0.001$) and WT and ΔE746-E750 ($p<0.001$), while there was no statistical difference between the two mutants L858R and ΔE746-E750 ($p=0.6364$).

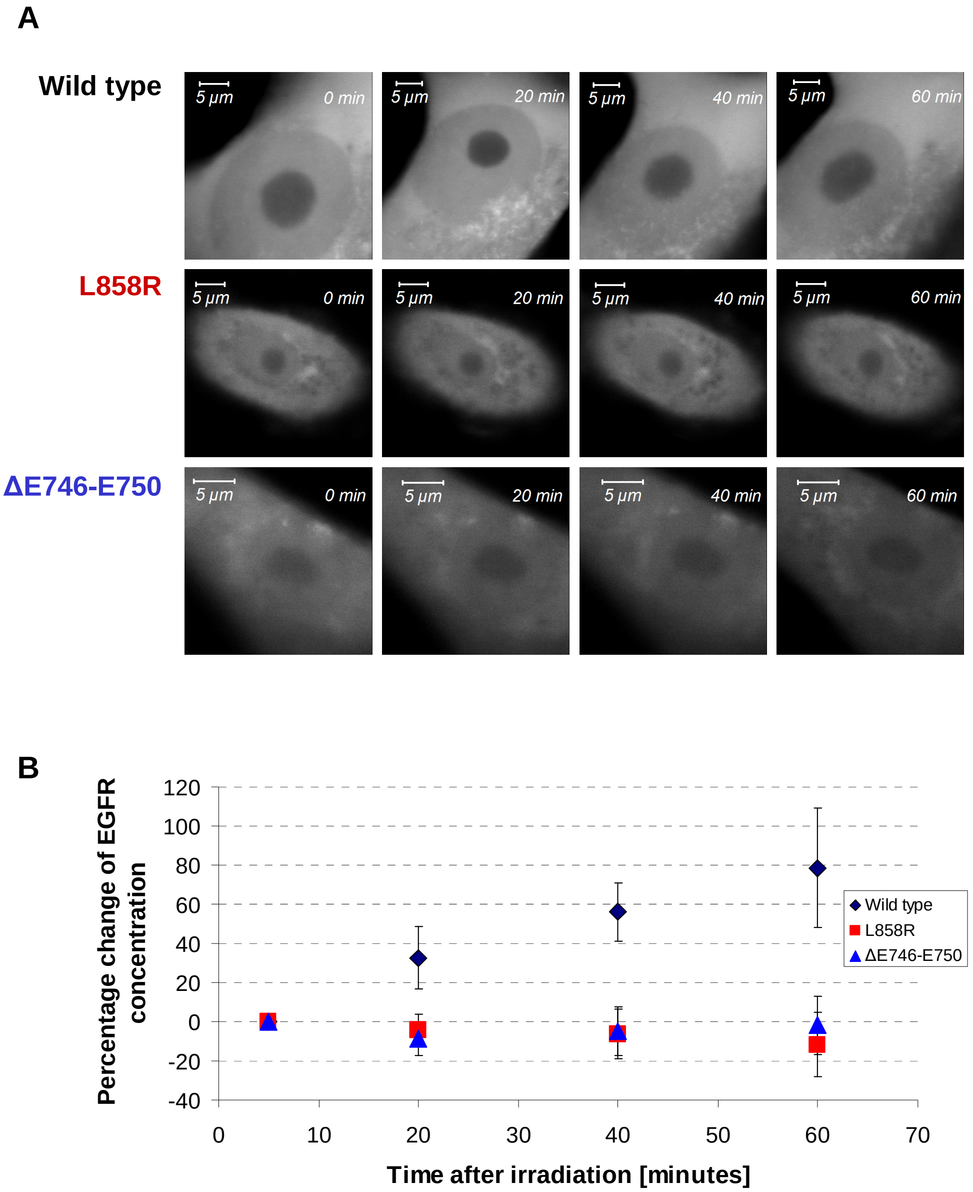

Figure 3.2 (A) Images of the relative fluorescence intensity in the cytosol versus the nucleus for WT and mutant DsRed-EGFR expressing HBEC cells before, and at different time points after 4 Gy γ-irradiation. (B) Percentage change in EGFR concentration (WT – diamonds, L858R – squares, ΔE746-E750 – triangles) as a function of time after 4 Gy γ-irradiation. The error bars represent SD calculated from ten different cells.

3.3.2 Effect of cetuximab on the γ-irradiation induced translocation of wild type and mutant EGFR in HBEC cells

Next, we examined the effect of cetuximab on the nuclear translocation of WT DsRed-EGFR and its mutants as a function of time after 4 Gy of γ-irradiation. Stable transfectants of WT, L858R and ΔE746-E750 were treated with cetuximab (100µg/ml) for 8 hrs and then irradiated with 4 Gy. Stacks of 50 images were taken at 5, 20, 40 and 60 minutes after irradiation for each cell. It was found that in stable HBEC WT cells (n=10) the nuclear EGFR concentration increased to ~ 26% at the one-hour point relative to the five-minute point post-irradiation (Fig. 3.3a). The accumulation of nuclear WT-EGFR was statistically significant with respect to the mutants ($p<0.001$, for both WT versus L858R and WT versus ΔE746-E750 comparisons). On the other hand, there was no statistically significant change in nuclear EGFR levels for the L858R and ΔE746-E750 cell lines ($p=0.3490$, for a paired comparison between these two mutants, L858R and ΔE746-E750). When comparing WT-EGFR without cetuximab, translocation reached ~80% at about 1 hour after 4 Gy γ-irradiation, while WT-EGFR with cetuximab treatment resulted in ~26% translocation after the same time interval (Fig. 3.3b).

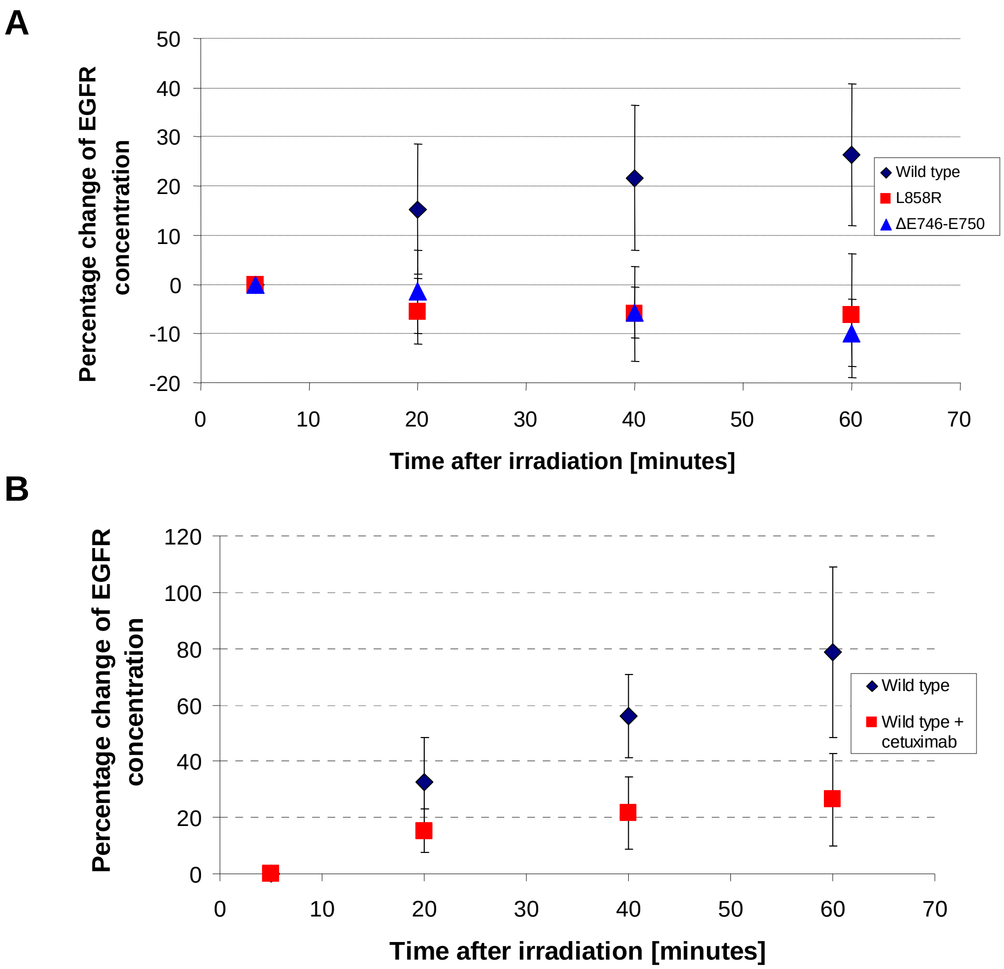

Figure 3.3 (A) Percentage change in EGFR concentration (WT – diamonds, L858R – squares, ΔE746-E750 – triangles) at different points after cetuximab and irradiation. (B) Percentage change in EGFR concentration in the nucleus for WT-EGFR (WT – diamonds, WT + cetuximab – squares) after a dose of 4 Gy as a function of time up to one hour after irradiation. The error bars represent SD calculated from ten different cells.

3.3.3 Effect of mutant EGFR on the nuclear translocation of wild type EGFR after γ-irradiation

In order to study the effect of mutant EGFR on the translocation of WT-EGFR to the nucleus, transient transfections of EGFP-EGFR (WT) were performed in HBEC cells with stable expression of one of several DsRed-EGFR variants (WT, L858R and ΔE746-E750) and, subsequently, changes in nuclear EGFP-EGFR concentration were monitored as a function of time post-irradiation. The results in Fig. 3.4 indicate that there was a nuclear translocation increase of EGFP-EGFR in WT background cells (n=10) by ~37% after one hour post 4 Gy γ-irradiation, with respect to the five-minute timepoint. There was also a statistically significant change of EGFP-EGFR concentration between WT and L858R (p<0.001) and WT and ΔE746-E750 (p<0.001). On the other hand, there was no statistically significant change of EGFP-EGFR levels between the L858R and ΔE746-E750 cell lines (p=0.2381), analysis was performed using mixed linear model analysis [68].

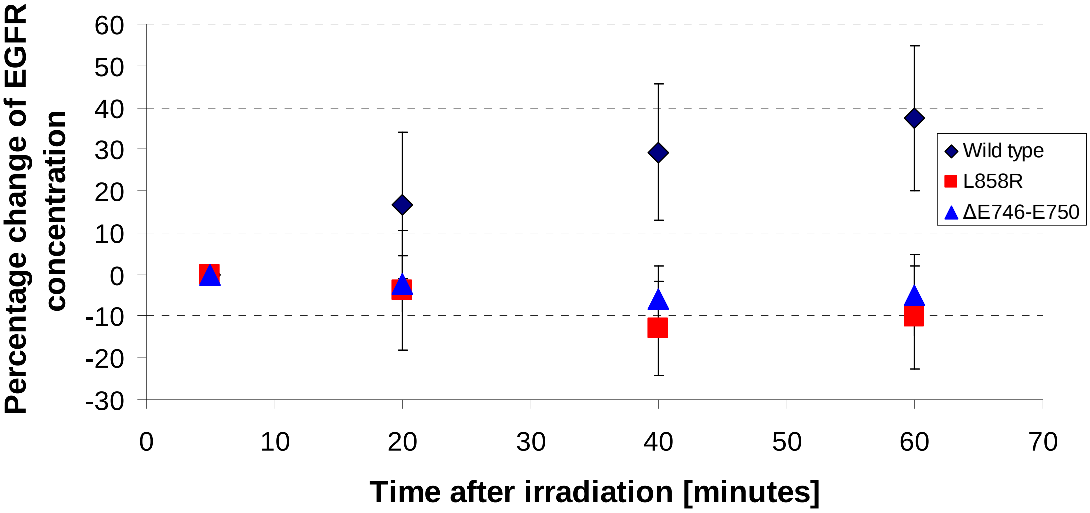

Figure 3.4: Percentage change in the nuclear EGFP-EGFR concentration in HBEC cells with different DsRed-EGFR backgrounds (WT – diamonds, L858R – squares, ΔE746-E750 – triangles) as a function of time after dose of 4 Gy. The error bars represent SD calculated from ten different cells.

3.4 Conclusion

The epidermal growth factor receptor (EGFR), which is over-expressed in tumors cells of epithelial origin is one of the determinants of tumor responses to ionizing radiation. Recently, it has been shown that higher EGFR expression levels lead to higher tumor resistance to radiation therapy through the activation of cell proliferation and survival pathways. In this study, a raster-scan imaging technique known as Number and Brightness (N&B) analysis has been employed to demonstrate the nuclear translocation of EGFR in living cells under a variety of experimental conditions. About 80% of wild type (WT) EGFR translocated to the nucleus after γ-irradiation while the L858R and ΔE746-E750 mutant EGFR did not. Subsequently, the effects of γ-irradiation together with an EGFR-blocking antibody (cetuximab) were monitored simultaneously in the same cell lines expressing EGFR and its mutants. In the combined radiation and cetuximab treatment, about 26 % of WT were translocated to the nucleus, while the L858R and ΔE746-E750 mutant EGFR did not. These results are consistent with findings attained by standard molecular techniques and support the hypothesis that a cytosolic pool of EGFR exists that cannot be accessed by cetuximab and can therefore contribute to treatment resistance.

CHAPTER 4

IN VITRO BINDING KINETICS OF DNA DOUBLE STRAND BREAK REPAIR PROTEINS KU70/80 AND DNA-PKCS QUANTIFIED BY FLUORESCENCE CORRELATION SPECTROSCOPY AND FLUORESCENCE CROSS-CORRELATION SPECTROSCOPY

4.1 Introduction

Genomes and their precursor nucleotides in both eukaryotic and prokaryotic cells are usually exposed to reactive oxygen species (ROS) as byproducts of oxygen metabolism [69, 70] which leads to DNA damage. Genomic corruption can also be caused by exposure to external factors such ionizing radiation [71, 72] UV-radiation and radio mimetic chemicals. The genomic integrity of cells is especially at risk when both phosphate backbones are severed, since this event results in breakage of the entire chromosome. Chromosome breakage presents a major challenge for cell division [11, 73]. During division, chromosome fragments can be distributed unequally over daughter cells or they can be translocated to places in the genome where they do not belong. In many cases, cells that are the victim of such an attack suffer death. But in the worst case scenario, deletion or translocation of chromosome fragments leads to inactivation of tumor suppressor genes or activation of oncogenes. Both events can trigger the onset of carcinogenesis in surviving cells [74]. Unrepaired double strand break (DSB) can have serious effect in dividing cells. The cell needs to take rapid counter measures first, to stop or delay cell division and second to repair the DSB.

There are different forms of DNA damage that occur in eukaryotic and prokaryotic cells, out of all these damages, the most lethal one is DNA DSBs (double strand breaks). There are two main pathways to repair DNA DSBs; homologous recombination (HR) and non-homologous end joining (NHEJ) [64, 75]. HR repairs the damage with high fidelity because it uses a template to repair the damaged nucleotides, while NHEJ is prone to error because it does not have a template to follow. In simpler organisms HR is the main DNA damage repair mechanism while in higher eukaryotes, especially humans, NHEJ is the predominant repair mechanism. Up to now, there are no clear mechanisms that identify as to why the cell will choose one pathway or the other, but it has been shown that cell cycle control of DNA end resection influences the choice between these two DSB repair pathways [76-79]. The following proteins play a major role in NHEJ: Ku70/Ku80 heterodimer, DNA-PKcs, XRCC4 (X-ray cross complementing 4), DNA ligase IV, Artemis and XLF (XRCC4-like factor) [80, 81]. The NHEJ pathway has three major steps: the first is recognition of the DNA break, the second step is DNA processing in order to remove non-ligatable ends and thirdly ligation of the DNA ends is effected. NHEJ is a complex process and requires a tightly coordinated interplay between key enzymes and repair proteins to timely initiate each subset of the entire process [75]. After a DNA DSB is caused by either an external or an internal factor, the Ku70/80 heterodimer acts as a sensor for DSB recognition. Ku70/80 then recruits DNA-PKcs as one of the key protein that regulating the formation of molecular complexes that process and repair the DSBs. Different processing factors like Artemis are recruited depending on the complexity of the damage termini. Interaction of DNA-PKcs molecules on adjacent sides of the DSB stimulates the protein kinase activity of DNA-PKcs, leading to DNA-PKcs autophosphorylation. In addition to DNA-PKcs, Ku70/80 also recruits XRCC4 DNA ligase IV, Artemis, XLF. The final step in NHEJ is DNA ligation, which is carried out by the XRCC4/DNA ligase IV complex[4].

The DSB binding kinetics of most of the above-mentioned repair proteins have not been fully investigated. In this work we studied the binding kinetics of the first two proteins, namely Ku70/80 and DNA-PKcs, interacting together with dsDNA, which mimicked DSBs. FCS/FCCS measurements were performed in order to estimate the minimum DNA base-pair (bp) length that Ku needed to bind effectively onto a dsDNA fragment. Different lengths of dsDNA were used: 25 bp, 33 bp and 50 bp. It has been found that increasing the salt concentration weakened binding of Ku to dsDNA. In fact, as the 25 bp binding was weak even at physiological salt concentrations, it was not possible to quantify the K_d at higher salt concentrations. Also, it was observed that the binding constant per binding site remained constant for 33 and 50 bp dsDNA strand lengths. A competition study was also performed to verify the specificity of DNA-Ku binding kinetics. Cy5-DNA and GFP-Ku70/80 were mixed and incubated for about 20 minutes in order to attain binding equilibrium and then different concentrations of unlabeled Ku70/80 were used to compete for DNA binding sites with the labeled counterpart. Finally, using FCCS it was possible to estimate the apparent K_d value for DNA-PKcs binding onto the DNA-Ku70/80 complex and the induced dissociation of DNA-PKcs from that complex by phosphorylation was observed in real time with this technique.

4.2 Materials and Methods

4.2.1 dsDNA Duplexes

The duplexes of blunt-ended DNA were made by annealing the labeled oligonucleotides (Operon, Huntsville, AL) with their complementary unlabeled oligonucleotides (Invitrogen, Grand Island, NY). The ends of oligonucleotides were labeled with Cy5. The annealing process of complementary strands was performed by heating at 95 ℃ for about 3 min and then slowly decreasing the temperature to 60 ℃. Then the sample was kept in a water bath at 60 ℃ for about one hour and then allowed to cool down to room temperature. The concentration of unlabeled oligonucleotides was 10 % more than that of labeled oligonucleotides in all annealing reactions. The 50 bp oligonucleotide 5’-CAGTGAATGG AATGCCTCTC AATTTTCTTG AAGACGCACA GTTTTCTCAG-3’ was annealed with complimentary 50bp [Cy5]CTGAGAAAAC TGTGCGTCTT CAAGAAAATT GAGAGGCATT CCATTCACTG. The 25bp oligonucleotide 5’-CAGTGAATGG AATGCCTCTC AATTT was annealed with complimentary 25bp [Cy5]CTGAGAAAAC TGTGCGTCTT CAAGA. The 33bp oligonucleotide 5’-GAGAAAACTG TGCTTCTTCA AGAAATTGAG AGG-3’ was annealed with complimentary 33bp [Cy5]CCTCTCAATT TCTTGAAGAA GCACAGTTTT CTC-3’.

4.2.2 GFP-Ku70/80 and Cy5-dsDNA interaction

33bp dsDNA: The sample was prepared by adding 6.6 µl of distilled water, 1 µl Ku-buffer (250 mM HEPES, 800 mM KCl, pH 7.6), 1 µl of 0.84 nM 33 bp Cy5-dsDNA and 1.4 µl of 1.4 µM GFP-Ku70/80. Then the sample was incubated at room temperature for about 20 minutes in the dark. Then 190 µl of Ku-buffer (80 mM KCl) was added. The sample was pipetted in the eight-well Lab-Tek chamber and 10 FCS measurements were taken, each with 10 seconds of measurement time. The same procedure was repeated for a salt concentration of 150mM, 220 mM and 300 mM. *25bp dsDNA*: The sample was prepared by adding 7 µl of distilled water, 1 µl Ku-buffer (250 mM HEPES, 800 mM KCl, pH 7.6), 1 µl of 0.8 nM 25 bp Cy5-dsDNA and 1µl of 1.4 µM GFP-Ku. The rest of the procedures were as for the 33 bp dsDNA, above. *50bp dsDNA*: The sample was prepared by adding 7 µl of distilled water, 1 µl Ku-buffer (250 mM HEPES, 800 mM KCl, pH 7.6), 1 µl of 0.05 nM 50 bp Cy5-dsDNA and 1 µl of 1.4 µM GFP-Ku. The rest of the procedures were as for the 33 bp dsDNA, above.

4.2.3 Competitive binding of unlabeled Ku70/80 with GFP- Ku70/80 and Cy5-DNA and effects of DNA-PKcs and ATP on the Ku70/80-DNA interaction

The sample was prepared by adding 7 µl of distilled water, 1 µl Ku-buffer (250 mM HEPES, 800 mM KCl, pH 7.6), 1 µl of 0.84 nM 33 bp Cy5-dsDNA and 1 µl of 1.4 µM GFP-Ku70/80. Then the sample was incubated at room temperature for about 20 minutes in the dark. Then 190 µl of Ku-buffer (80 mM KCl) was added. The sample was pipetted in the eight-well Lab-Tek chambered and 10 FCS measurements were taken. Then 1 µl of unlabelled Ku70/80 (1.67 µM) was added in the sample and 10 FCS measurements were taken. Then another 4 µl of unlabelled Ku70/80 (1.67 µM) was added in the sample and 10 FCS measurements were taken. For the experiments involving DNA-PKcs, 5 µl of 0.7µM DNA-PKcs was added to the equilibrated Ku-DNA solution and 10 FCS measurements were taken. Then 16 µl of ATP (25mM) were added and 10 FCS measurements were taken. In all cases each one of the FCS measurements lasted 10 seconds.

4.2.4 Effects of PKcs and ATP in Ku and DNA interaction

The sample was prepared as described in sub-section 4.2.3, above, up to and including the pint where 1 µl of unlabelled Ku (1.67 µM) was added. Then 5 µl of 0.7µM DNA-PKcs was added and 10 FCS measurements were taken, each with 10 seconds measurement time. To demonstrate the effect of DNA-PKcs phosphorylation on the binding kinetics with the Ku70/80-DNA reaction product, 16 µl of ATP (25mM) were added and 10 FCS measurements were taken, each with 10 seconds measurement time.

4.2.5 FCS experimental setup

FCS measurements were performed using the ConfoCor 3, Version 4.2 (Carl Zeiss MicroImaging GmbH, Jena, Germany) with a 40x water immersion C-Apochormat objective lens of 1.2 N.A.. The sample was placed inside an eight-well Lab-Tek chambered borosilicate coverglass (Nalge Nunc International). Calibration for the green channel was performed using 4 nM Rhodamine-6G with a known diffusion coefficient of 2.8 x 10^{-10} m^2/s. Using this calibration information the confocal volume was calculated to be 0.34 fl. Before calibration, pinhole were adjusted as shown in appendix C. Calibration for red channel was performed using 10 nM Cy5 with a known diffusion coefficient of 3.13 x 10^{-10} m^2/s, which led to a calculated confocal volume size of 0.74 fl. As the focal volume size was a function of wavelength, the cross correlation volume was calculated as an estimate of the mean overlap volume for the two wavelengths and the effective volume for the cross-correlation was ~0.53 fl [82].

4.3 Theoretical Calculation of the Diffusion Coefficient for Spherical and Linear Molecules

For Ku70/80 and DNA-PKcs proteins, the diffusion constants were calculated assuming globular macromolecules, the diffusion constant is given by

$$D = \frac{k*T}{6*\pi*\eta*r} \tag{4.1}$$

Where *k* is Boltzmann constant, *T* is absolute temperature, *η* is viscosity, *r* is the hydrodynamic radius of the globular molecule given by the following equation [82]:

$$r = \left[\frac{\left(3 * m \Big/ N_A \right)}{4 * \pi * \rho} \right]^{1/3} \tag{4.2}$$

Where *m* is the molecular mass of the globular molecule, N_A is the Avogadro's number, *ρ* is the density of the protein molecules.

For DNA molecules, the translational diffusion coefficient of DNA molecule is given by the following equation

$$D = \frac{A * k * T}{3 * \pi * \eta * L} \tag{4.3}$$

Where *k, T* and *η* same as Eq. 4.1, while *L* is the length of DNA and *A* is correction factor given by the following formula [82]:

$$A = In(\frac{L}{d}) + 0.312 + \frac{0.565}{(L/d)} - \frac{0.1}{(L/d)^2} \tag{4.4}$$

Where *d* is the diameter of the rod (linear DNA).

The DNA-Ku reaction can be represented by [82]:

$$DNA + Ku \leftrightarrow DNA\text{-}Ku \tag{4.5}$$

The association constant *K*, is given by the following equation [82]:

$$K = \frac{[Ku - DNA]}{[Ku] * [DNA]} \tag{4.6}$$

Where *[Ku]* is the concentration of Ku, *[DNA]* is the concentration of DNA and *[Ku-DNA]* is the concentration of Ku and DNA.

But K is equal to $1/K_d$, where K_d is dissociation constant, therefore

$$K_d = \frac{[Ku]*[DNA]}{[Ku - DNA]} \tag{4.7}$$

For dissociation constant, K_d for DNA-Ku and PKcs interaction

The DNA-Ku and PKcs reaction can be represented by:

$$\text{DNA-Ku} + \text{PKcs} \leftrightarrow \text{DNA-PKcs} \tag{4.8}$$

The association constant K, is given by the following equation:

$$K = \frac{[DNA - PKcs]}{[DNA - Ku]*[PKcs]} \tag{4.9}$$

Where *[PKcs]* is the concentration of PKcs, and *[DNA-PKcs]* is the concentration of DNA-PKcs complex. Dissociation constant, K_d for DNA-Ku and PKcs interaction is given by:

$$K_d = \frac{[DNA - Ku]*[PKcs]}{[DNA - PKcs]} \tag{4.10}$$

4.3.1 Data analysis for FCS

The correlation of fluorescence intensity fluctuations $\delta I(t)$ resulting from diffusing fluorescent molecules in the confocal volume when fluorescence intensity fluctuations after time $(t + \tau)$ yield the normalized intensity autocorrelation function $G(\tau)$:

$$G(\tau) = 1 + \frac{<\delta I(t)\delta I(t+\tau)>}{<I>^2} \tag{4.11}$$

where the brackets describe the time average and <*I*> the mean fluorescence intensity [83, 84]. The translational diffusion due to the Brownian motion of the protein molecules in a 3D Gaussian volume is give by [85]:

$$G\ (\tau)=1/N\left[\sum_{i=1}\frac{\phi_i}{\left(1+\left[\tau\Big/\tau_{d,i}\right]^{\alpha_i}\right)^{e_{d1}}\left(\left(1+\left[\tau\Big/\tau_{d,i}\right]\alpha_i\,.\,1\Big/s^2\right)^{1/2}\right)^{e_{d2}}}\right] \qquad (4.12)$$

with the constraint $\Sigma_i \Phi_i=1$, $\tau_{d,i}$ representing the diffusion time of species I and α_i representing the anomalous diffusion parameter (for free diffusion $\alpha=1$). *S* is the structure parameter [40, 86], $S=z/\omega$, where ω denotes the $1/e^2$ radius of the 3D Gaussian confocal volume, *z* is axial radius of confocal volume and $\tau_d=\omega^2/4D$ where *D* is the diffusion coefficient [87, 88].

Multiple diffusive components were considered to accommodate for the simultaneous presence of monomers, multimers and free dye that could possibly coexist within the confocal volume. To reduce the number of fitting components the free dye and monomer coefficients were determined independently in prior experiments and were kept fixed during the fitting of the reaction data. FCCS measurements were employed to determine the complex concentrations [AB], e.g. [DNA-Ku], and FCS to determine the monomer concentrations [A] and [B], e.g. [DNA] and [69]. The K_d of the reaction was subsequently calculated as [A][B]/[AB] [89].

4.4 Results and Discussion

4.4.1 FCCS Based Quantification of DNA-Ku Binding Kinetics

FCS/FCCS curve amplitudes attain a maximum autocorrelation value of $G(\tau=0)-1$ and decay towards zero at longer correlation times τ. The detailed shape of these curves depends on the underlying biophysical forces that drive the transit of fluorescently labeled molecules through the confocal volume e.g. diffusion and binding kinetics. In FCS the G(0)-1 value is inversely proportional to N [90], the average number of molecules occupying the confocal volume during the measurement period (100 sec). All measurements were performed after ample time (~20 minutes) was allowed for the DNA-Ku kinetics in solution to reach equilibrium, as verified by repeated measurements at increasing time intervals post-incubation. The Ku molecule had a much larger molecular weight (177kD) compared to the dsDNA fragments (16.5-33 kD) and the bound dsDNA fraction was observed through a change in the DNA apparent diffusion coefficient that matched the theoretically predicted value for the Ku-DNA complex. The latter was more massive than unbound DNA and therefore diffused more slowly. Diffusion coefficients values could be inferred by fitting the experimental curves to appropriate models for multi-component diffusive transport [88], as described in sub-section 4.3.1 above.

Double stranded DNA fragments were labeled by Cy-5 and are depicted as red curves in Figure 4.1. Ku was expressed as a fusion protein with GFP and its autocorrelation curves are shown in blue. The black curves show the cross-correlation signal resulting from coincident green and red fluorescence fluctuations for Ku and DNA, respectively. FCS/FCCS measurements were performed to explore the minimum base-pair (bp) length that Ku needed as a foothold to bind effectively onto the tips of different length dsDNA fragments, simulating DSBs. Figs 4.1(a) and (b) show binding of Ku at the same salt concentration of 80mM. The corresponding K_d values are highlighted in yellow in Table 1. Clearly 25 bp is not sufficient for Ku to have a full foothold as demonstrated by the weaker binding (higher K_d values). This finding is supported by independent evidence from previously reported light scattering experiments [91]. We also performed measurements at salt concentrations of 80, 150, 220 and 300 mM to demonstrate the difference in K_d as a function of the solution's ionic strength i.e. conformation based versus electrostatic binding (physiological range is 80-130 mM). We found that increasing the salt concentration weakened binding of Ku to DNA (Table 4.1). In fact, as the 25 bp binding was weak even at physiological salt concentrations, it was not possible to quantify the K_d at higher concentrations. We also see from Table 4.1 that the binding constant per binding site remains constant for 30 and 50 bp dsDNA strand lengths. The K_d values reported in

Table 4.1 are in agreement with previously reported values for DNA-Ku interactions determined by other biophysical methods at comparable physiological conditions [92].

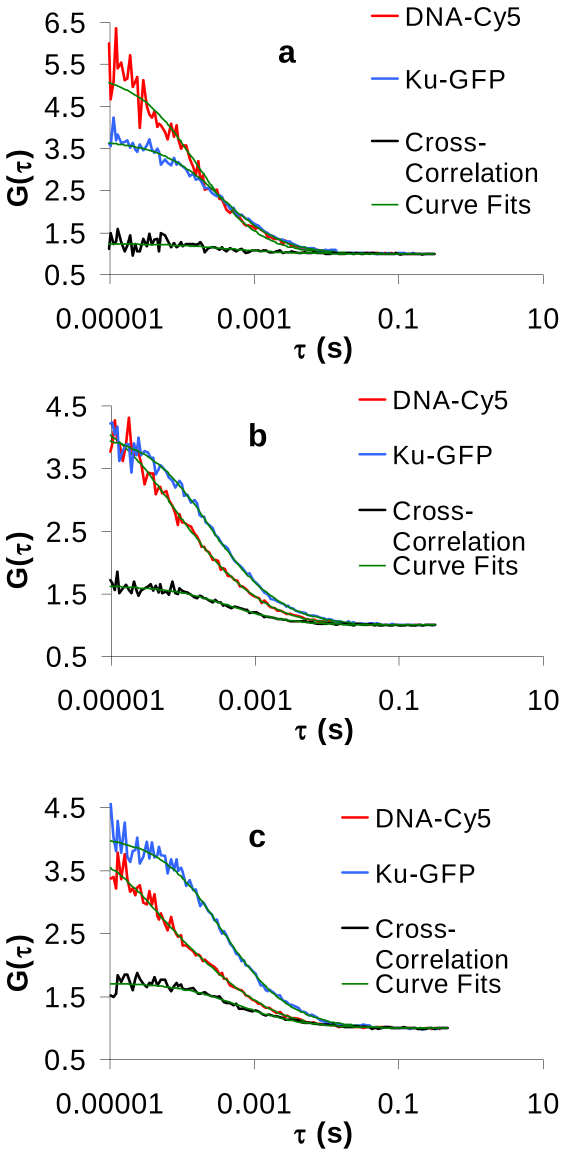

Figure 4.1 Autocorrelation and cross-correlation curves demonstrating Ku-GFP and dsDNA-Cy5 interaction in KCl solution (a) 25pb ddDNA in 80mM KCl, (b) 33pb ddDNA in 80 mM KCl (c) 50pb ddDNA in 150mM.

Table 4.1 Different dissociation constant of Ku-DNA with different length of the DNA and dependence of dissociation constant on different salt concentrations

dsDNA length	K_d [nM]			
	80 mM KCl	150 mM KCl	220 mM KCl	300 mM KCl
25 bp	0.29 ± 0.17	-	-	-
33 bp	0.12 ± 0.04	0.16 ± 0.09	0.41 ± 0.07	21.65 ± 4 .58
50 bp	*0.11 ± 0.05*	0.09 ± 0.03	*0.52 ± 0.20*	18.06 ± 1.10

4.4.2 FCS Based Competition Studies on Ku-DNA Binding

A competition study was performed to demonstrate the specificity of DNA-Ku binding. After DNA-Cy5 and Ku-GFP at 1:1500 molar ratio were mixed and left to incubate until equilibrium (please see Section D for Details) different amounts of unlabeled Ku competitor were added to the solution. A competitor would be unable to displace a labeled ligand from a non-specific binding site because non-specific binding is not mediated by structural recognition of the ligand, and it is exactly that structural recognition which is shared with the competitor. Incremental addition of unlabeled Ku (Ku-GFP/unlabeled Ku molar ratios of 1 and 5, 1 μl and 4 μl respectively) reduced the DNA-Ku cross-correlation amplitude down to nearly zero (Fig. 4.2) which corresponded to nearly complete replacement of Ku-GFP with unlabeled ligand. These experiments demonstrated the specificity of binding at a physiologically relevant salt concentration.

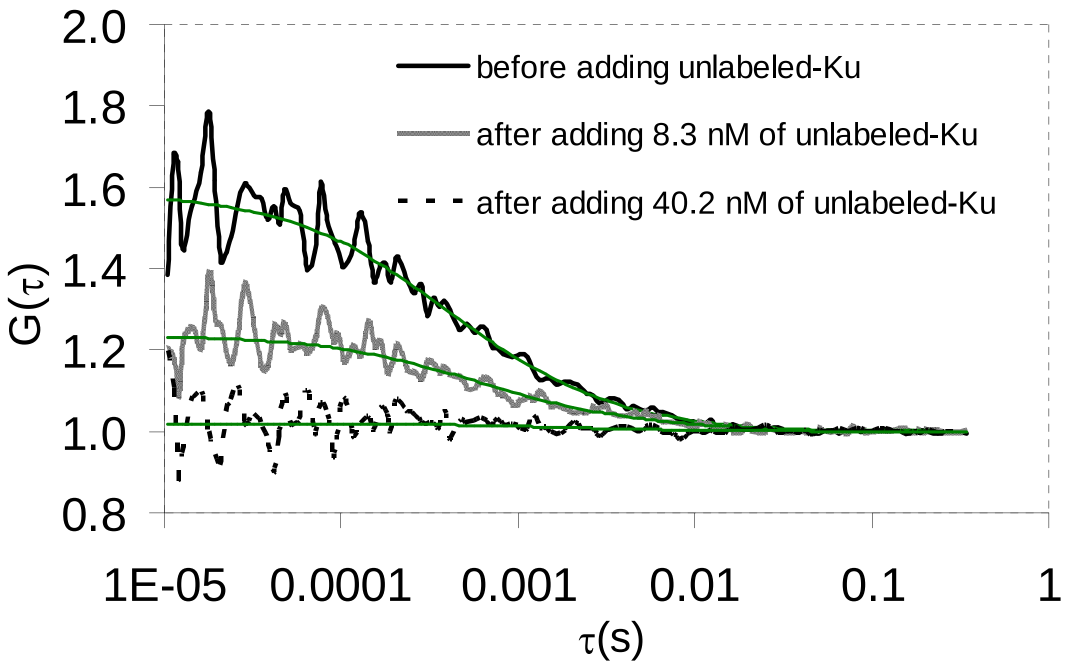

Figure 4.2 Cross-correlation curves for GFP-Ku and 33 bp Cy5-dsDNA in 80 mM KCl. The net autocorrelation amplitude decreased to about 0.2 when 1ul of 1.67 µM unlabeled-Ku were added (8.3 nM of unlabeled Ku). After addition of 4 µl of 1.67 µM unlabeled Ku (40.2 nM of unlabeled Ku) the cross-correlation amplitude decreased to almost zero.

4.4.3 FCCS Based Quantification of PK_{CS} Binding onto the DNA-Ku complex

After letting dsDNA-Cy5 and Ku-GFP equilibrate in solution (Fig. 4.3a), unlabeled DNA-PK_{CS} was added (DNA-PK_{CS}/ Ku-GFP molar ratios of 2) and, as a result slow moving multimers with a diffusion coefficient in vicinity of 2.3 x 10^{-11} m^2/s were observed (Fig. 4.3b). Subsequent addition of ATP reverted the observed diffusion coefficients back to DNA-Ku and PKcs monomer values (Fig. 4.3c). Unbinding of DNA-PKcs after addition of ATP was confirmed by an increase of the apparent DNA and Ku concentrations (observed through the red and blue FCS channels, respectively), as witnessed by the reduced G(0) values in Fig. 4.3c relative to Fig. 4.3b. Unbinding of DNA-PKcs from the DNA-Ku complex upon phosphorylation had been directly observed previously [22]. These findings show the power of FCS/FCCS measurements to monitor aggregation and disaggregation of macromolecular complexes relevant to DNA repair in real time.

In addition to monitoring aggregation/disaggregation the above measurements also enabled us to estimate the apparent K_d value for DNA-PKcs binding onto DNA-Ku, which is currently not reported in the literature. We refer to this K_d estimate as ‘apparent’ because there are three distinct molecular species involved in this reaction, whereas the typical K_d definition refers to interaction between only two interacting partners [93]. The implicit assumption made to perform this K_d estimate was that Ku binds more strongly to DNA than PKcs does on Ku or DNA alone. This is a reasonable assumption since Ku is known to be the first response DSB recognition molecule that stays at the DNA damage spot throughout the repair process while PKcs has a shorter residence time at DSBs (Fig. 2). We therefore treat DNA-Ku as a single macromolecule and PKcs as the other binding partner, thus enabling estimation of the apparent K_d as [DNA-Ku][DNA-PKcs]/ [DNA-Ku – DNA-PKcs] (Table 4.2). We propose to pursue more detailed chemical kinetics modeling studies in the future, along the lines of Lieber *et al* [94], to extract a quantitative estimate for the true PK_{CS} K_d values. Interestingly, the current apparent K_d results imply (due to the inverse relationship between K_d and strength of binding) that upon phosphorylation PK_{CS} binds more strongly onto the DSB break, which is consistent with the current hypothesis that it serves as an anchor for other end-processing molecules to attach and process the DNA ends [75]. In addition, there is evidence that upon phosphorylation DNA-PK_{CS} makes a short step back and away from the DSB in order to make the dsDNA tips accessible to end-processing enzymes [95]. This behaviour is consistent with the ATP-induced multimer disaggregation that we observed in Fig. 4.3c.

Table 4.2. ATP concentration dependence of apparent K_d for DNA-PKcs binding onto the DNA-Ku complex

	K_d [nM] with ATP	K_d [nM] without ATP
[DNA-Ku]-DNA-PKcs	6.50±0.01	15.00± 0.01

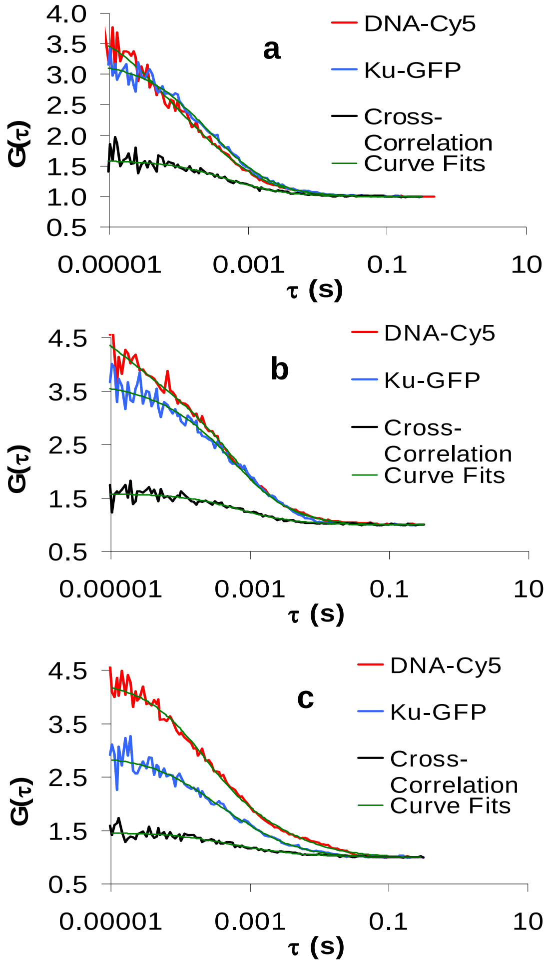

Figure 4.3 Changes in the binding of GFP-Ku to 33bp Cy5-dsDNA in 80 mM KCl in the presence of (a) 3.5 nM DNA-PKcs, (b) 17nM DNA-PKcs, and (c) after adding 1.9 μM ATP in the 17nM DNA-PKcs solution.

.

4.5 Conclusion

DNA double-strand breaks (DSBs) are one of the most lethal types of DNA damage that occurs in eukaryotic cells. There are two distinct pathways of repairing DSBs, homologous recombination (HR) and non-homologous end joining (NHEJ). In the NHEJ repairing pathway, DSB recognition and repair initiation is directed by the interaction of DNA-binding subunit Ku70/80 heterodimer with the DNA-PK protein catalytic subunit (DNA-PKcs). Mutations in these proteins result in repair stalling and eventual DNA misrepair that may lead to genomic instability. Studying the binding kinetics of these repair proteins is therefore important for understanding the conditions under which DSB repair stalls. Currently open questions are, what is the minimum DNA length that this complex needs to get a foothold onto a DSB and how tightly does DNA-PKcs bind onto the DNA-Ku70/80 complex. Fluorescence Correlation Spectroscopy (FCS) and Fluorescence Cross-Correlation Spectroscopy (FCCS) techniques have the potential to give information about the binding kinetics of DNA-protein and protein-protein interactions at the single-molecule level. In this work, FCS/FCCS measurements were performed to explore the minimum DNA base-pair (bp) length that Ku70/80 needed as a foothold to bind effectively onto the tips of different lengths dsDNA fragments that mimic DSBs. 25 bp, 33 bp and 50 bp of dsDNA were used for these experiments and binding was studied as a function of salt concentration in solution. It was found that the 25 bp binding was weak even at physiological salt concentrations while the dissociation constant (K_d) remained constant for 33 and 50 bp dsDNA strand lengths. These studies indicated that the minimum binding length for the Ku70/8 is in the vicinity of 25 bp. The specificity of binding of Ku70/80 was proven by competitive binding FCCS experiments between Cy5-labeled DNA, GFP-Ku70/80 and titrations of unlabeled Ku70/80. Finally, using FCCS it was possible to estimate the apparent K_d for DNA-PKcs binding to the DNA-Ku70/80 complex and the induced dissociation of DNA-PKcs from that complex by phosphorylation was observed in real time.

CHAPTER 5

SCANNING FLUORESCENCE CORRELATION SPECTROSCOPY TECHNIQUES TO QUANTIFY DNA REPAIR PROTEIN KINETICS AFTER γ-IRRADIATION AND BLEOMYCIN

5.1 Introduction

A DNA double-strand break (DSB) is one of the most lethal types of DNA damage occurring in eukaryotic cells [96]. Improper repair of DSBs may lead to mutations, chromosomal translocations, apoptosis, and genetic instability [97, 98]. Improper repair may also increase the probability of cancer [98] and of immune deficiencies [99]. There are two distinct pathways of repairing DSBs; homologous recombination (HR) [100] and non-homologous end joining (NHEJ)[101]. In the NHEJ repairing pathway, the DNA dependent protein kinase (DNA-PK) complex plays a major role in DSB recognition and coordination of subsequent repair steps. The DNA-PK complex consists of the catalytic subunit (DNA-PKcs) and the DNA-binding heterodimer subunit Ku70/80 [102, 103]. The Ku70/80 heterodimer is the first DSB recognition event and subsequently DNA-PKcs binds onto it [4, 64]. These two proteins act together to modulate the transient binding of a sequence of other repair proteins into a multi-component complex at DSBs [4, 64]. As the repair process gets completed DNA-PKcs and then Ku70/80 eventually get released from the DSBs. Mutations on phosphorylation sites in DNA-PKcs can alter its kinase activity and stall the DSB repair process so that DNA-PKcs and Ku70/80 stay localized longer at DSBs compared to the wild type (WT) DNA-PKcs case [22]. The temporal evolution of DNA repair protein kinetics after DNA damage represents a surrogate measure of repair status.

If repair proteins are tagged with a fluorescent protein then their residence times at damage sites can be quantified by time lapse imaging [22]. However, very few of the proteins involved in DNA repair, such as 53BP1 and γH2AX [1, 104], bind in high numbers per DSB and are therefore visible under a fluorescence microscope. Most proteins involved in DNA repair, including DNA-PKcs and Ku70/80, only bind to DSBs in few copies and are therefore not easily discernible in fluorescence microscopy images over a background of freely moving protein. For this reason the standard method of visualizing the recruitment of these repair proteins at DNA damage sites has been to induce damage by focused laser irradiation [22]. The high density of damage sites created this way results in localized fluorescent hot spots that are visible over the fluorescent background of mobile protein moving through the same space in the nucleus [22]. In addition, some quantitative aspects of binding to damage sites have been previously obtained by Fluorescence Recovery After Photobleaching (FRAP) applied onto a laser damage hot spot [22, 105]. However, it is of interest to study DNA repair kinetics under conditions that resemble more closely cancer treatment, such as by γ-irradiation or chemotherapy. In such cases, the induced DSBs are sparse and therefore not directly discernible in microscopy images.

In this work we present the application of two quantitative microscopy methods known as Number and Brightness (N&B) analysis [19, 47] and Raster-scan Image Correlation Spectroscopy (RICS) [9, 44] as means to address this challenge and quantify DNA repair protein kinetics after sparse damage. N&B analysis quantifies the number of molecules per image pixel, effectively the concentration, and the fluorescence brightness per molecule [19] for the mobile population fraction of a molecule. On the other hand, RICS quantifies the molecular concentration and apparent diffusion coefficients of fluorescently tagged molecules within user-selected sub-cellular regions of interest [44]. Here, we have used N&B analysis to quantify relative changes in the bound fraction of fluorescently tagged Ku70/80 and DNA-PKcs, and RICS to quantify changes in the apparent diffusion coefficients of these two repair proteins, with time post-damage as the surrogate measures of repair status. The agents of sparse DNA damage creation were γ-rays and bleomycin, both of which are known to form predominantly DSBs.

The N&B and RICS methods are relatively recent extensions of the Fluorescence Correlation Spectroscopy (FCS) technique that can quantify the diffusion coefficient, binding kinetics, photo-physics and concentration of fluorescently tagged molecules [9, 19, 44, 47]. FCS has been previously applied to study nuclear protein interactions with DNA *in vitro* [93, 106] and in living cells [107]. The practical challenge of this work with respect to prior studies is that quantification of kinetics over time requires repeated measurements on the same cell, which we have found to result in significant photobleaching when the FCS technique is used. On the other hand, N&B and RICS are techniques where the focal volume is repeatedly scanned over a user-selected area, which results in significantly less photobleaching [19, 44].

To our knowledge, this work presents the first application of N&B and RICS to the quantification of DNA repair kinetics after sparse damage, though RICS has been suggested as a means of identifying the presence of DNA damage after UV light exposure [16]. In addition to quantifying repair kinetics for Ku70/80 and DNA-PKcs for γ-irradiation doses down to 1 Gy and for a wide range of bleomycin concentrations, we also present control experiments to verify that the expected changes in repair kinetics are observed when their ability to disengage from DSBs is inhibited. To that end, N&B analysis was applied to the post-irradiation kinetics of the 7A DNA-PKcs phosphorylation mutant and after Wortmannin exposure for Ku70/80 cells. For the case of γ-irradiation we also present comparisons with laser damage kinetics for the same cell lines.

5.2 Materials and Methods

5.2.1 Cell culture, γ-irradiation and bleomycin treatment

CHO V3 (DNA-PKcs null) cells stably expressing YFP-DNA-PKcs or its 7A phosphorylation mutant [22] were maintained in a Modified Eagle's Medium (Invitrogen, Carlsbad, CA) supplemented with 10% penicillin, 10% fetal bovine serum (FBS) and 250 µg/ml of G418. CHO Xrs6 cells stably expressing GFP-Ku80 were maintained in similar conditions as the DNA-PKcs cell lines. Cells were grown in 35-mm glass-bottom dishes (Mattek Cultureware, Ashland, MA) and were maintained in a humidified 5% CO_2 incubator at 37^oC. Measurements were taken two days following cell splitting, at a confluency of near 100%. During the measurements cells were maintained in a CO_2-independent medium (Invitrogen, Carlsbad, CA) at 37℃. DSB repair in GFP-Ku80 cells was inhibited by incubation with Wortmannin for 45 min after which the cells were washed and the media was replaced.

For the γ-irradiation experiments cells were irradiated inside the 35-mm dishes, including the microscope stage dish holder. This way the dish orientation was maintained thus enabling to identify the same cells post-irradiation quickly, typically within 3 min. The γ-irradiation doses were in the 1-10 Gy range and were delivered using a ^{137}Cs irradiator (Mark 1 irradiator, JL Shepherd & Associates, San Fernando, CA), which took about 20 sec, 1 min 40 sec, 2 min 30 sec and 3 min for 1, 5, 7, and 10 Gy, respectively. For the radiomimetic chemical treatments cells at near 100% confluency in 35-mm glass-bottom dishes were treated to various doses (25 μg/ml, 50 μg/ml and 100 μg/ml) of bleomycin (Sigma-Aldrich) mixed with CO_2-independent medium for 3 minutes. Subsequently, the cells were washed to remove bleomycin from the surfactant and were placed in fresh CO_2-independent medium for further imaging. There was no cell cycle synchronization before radiation or chemical treatment.

5.2.2 Confocal imaging

Fluorescence images were acquired using an LSM 510 META confocal microscope (Carl Zeiss, Jena, Germany). A 63x oil immersion Plan-Apochromat objective lens with a numerical aperture (N.A.) of 1.4 was used for all experiments. For the Xrs6 cells expressing GFP-Ku80, images were obtained using a 488 nm Argon laser. A dichroic mirror (HFT 488/543) was used to route laser excitation power onto the sample in an epifluorescence geometry. To exclude any excitation light leakage, a band pass filter (BA 505–530 IR) was used before a photomultiplier tube (PMT) detector. For V3 cells expressing YFP-DNA-PKcs cells, a 514 nm argon laser was used. Detection of fluorescence was performed through a dichroic mirror (HFT 488/514) and a band pass filter (BA 530–600 IR) in front of the PMT detector.

5.2.3 Fluorescence correlation spectroscopy (FCS)

The FCS signal originates from the transits of fluorescently tagged molecules through a confocal detection volume at low concentration, which create fluctuations in the detected fluorescence intensity in a manner dependent on the underlying molecular kinetics [35]. The fluorescence intensity fluctuations $\delta I(t)$, resulting from the fluorescent molecules transiting through the confocal volume, when correlated with fluorescence intensity fluctuations detected after time $(t + \tau)$ yield the normalized intensity autocorrelation function $G(\tau)$ as shown in Eq. 2.1. For the cell measurements performed in this work a standard two-component diffusion autocorrelation function in a 3-D Gaussian focal volume was used as shown in Eq. 2.2 [40, 108]. The mean molecular transit time through the confocal observation volume for each of these diffusing components is given by Eq. 2.3 [87, 88]. The average number of molecules, N, in the confocal volume is given by Eq. 2.4 and effective confocal volume is given by Eq. 2.5. FCS measurements were performed using the ConfoCor3 attachment of a LSM 510 META confocal microscope, (Version 4.2, Carl Zeiss MicroImaging GmbH, Jena, Germany) with a 40x water immersion C-Apochormat objective lens with a N.A. of 1.2. Calibration of the confocal volume size for the green channel was performed using 4 nM of Rhodamine 6 Green placed inside eight-well Lab-Tek chambered borosilicate coverglass chambers (Nalge Nunc International). Using the known diffusion coefficient of 2.8×10^{-10} m^2/s for this fluorophore and fitting to a one-component diffusion model [109, 110] resulted in a confocal volume 0.34 fl. Specifically, he radial axis dimension, ω, was 0.23μm and the axial dimension z was 1.15 μm, making S equal to 5. For Xrs6 cells expressing GFP-Ku80, measurements were obtained using the 488 nm argon laser line with ~4 μW at the focal spot. A dichroic mirror (HFT 488/543) was used for separating the laser excitation beam from the collected fluorescence emission, and an excitation cut-off filter (NFT 500) was used before signals were directed to an avalanche photodiode (APD) detector. For V3 cells expressing YFP-DNA-PKcs, measurements were obtained with the 514 nm argon laser with ~3 μW at the focal spot. In this case, a different dichroic mirror (HFT 458/514) was used to separate laser excitation from fluorescence emission, and a band pass filter (BP 530-610 IR) was used to shield the APD from any excitation light leakage.

5.2.4 Number and Brightness (N&B) analysis

N&B analysis is based on the detection of time-series fluorescence signals as an image is raster-scanned, to deduce information about the effective molecular concentration and the agglomeration status of fluorescently tagged proteins [45, 47, 48]. In a given pixel obtained from the raster scan image, the apparent brightness (B) and apparent number of molecules (N) are related to signal variance (σ^2) and average intensity ($<k>$) as shown in Eq. 2.12 and Eq. 2.13. However, these B and N values contain signal fluctuation contributions both due to molecular mobility as well as due to detector shot noise and the immobile molecule background. The background-corrected quantities indicating the actual number of molecules (n) and molecular brightness (ε) are given Eq. 2.14 and Eq. 2.15 respectively. Confocal images for N&B analysis were acquired following previously published image acquisition parameters [19] with the aforementioned LSM 510 META microscope and ConfoCor3 attachment. The scan speed was set to 12.79 μs/pixel, corresponding to 1.38 s per frame, with each frame being 256 x 256 pixels (0.2 μm pixel size). A stack of 50 images was acquired for each measurement. Control experiments were performed to verify that N&B analysis could recover a known concentration of fluorescent bead solutions and verify that these were nearly monomeric after sonication. Green fluorescent beads of 25 nm diameter (Duke Scientific, Palo Alto, CA) at different dilutions from a stock solution of known concentration, placed in Lab-Tek chambered borosilicate coverglass wells (Nalge Nunc International, Rochester, NY), were used for these control experiments. A visual example of how n and ε were obtained from the raster-scanned images is shown in Fig. 5.1.

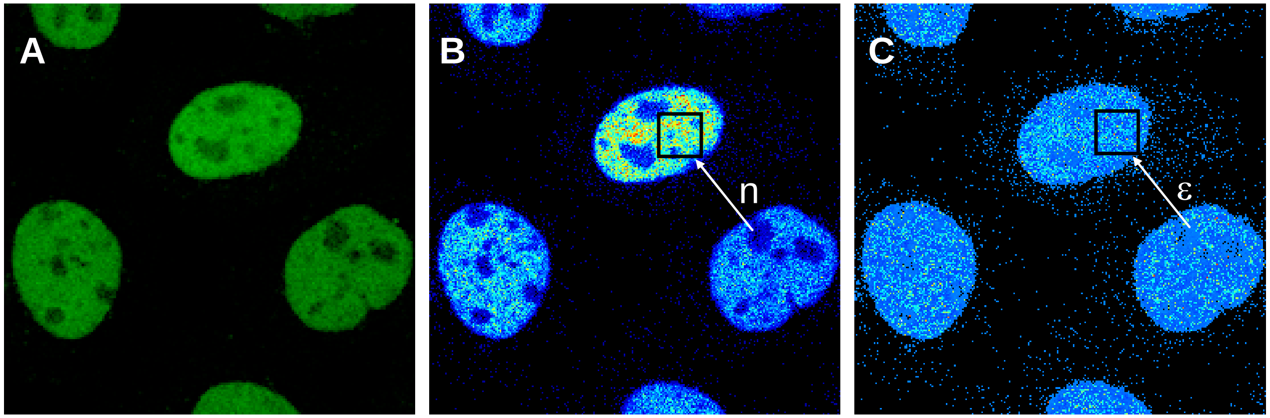

Figure 5.1: (A) Fluorescence intensity image of Xrs6 cells expressing GFP-Ku80; (B) The molecular number (*n*) image obtained after processing the image in (A) with Eq. 5.7. The inset (arrow) indicates a typical user-selected ROI between nucleoli the average value of which was used for subsequent mobile fraction calculations; (C) The molecular brightness (ε) map, obtained after processing the same image in (A) with Eq. 5.8, indicating even molecular brightness throughout the nucleus despite differences in protein concentration between cells, seen in (A) and (B).

5.2.5 Calculation of relative changes in the protein mobile fraction after DNA damage by combining N&B analysis with Strip-Fluorescence Recovery after Photobleaching (Strip-FRAP)

For live cell experiments, the above described N&B image acquisition settings enabled simultaneous collection of data from three or four neighboring cells that could fit in the field of view at any one time. These cells were selected to have a fluorescently tagged protein concentration in the 50-500 nM range as verified by sample FCS measurements. Higher concentrations produced very low amplitude FCS curves and very low N&B analysis signals. The lower bound in this concentration range was set by the expression levels of the cells and was measurable by both techniques. Also, in order to remove the immobile fraction of protein prior to irradiation, which was necessary for avoiding the mobile fraction signal to be overwhelmed, pre-bleaching was performed by taking 50 images using the same parameters as the ones used for all measurements. Subsequently, the cells were ready to be imaged just prior to, and as a function of time after, DNA damage was created by exposure to γ-irradiation or bleomycin.

For the case of γ-irradiation, a stack of 50 images was acquired just prior to exposure and then the cells were irradiated with doses in the 1-10 Gy range and brought back from the irradiator room into the neighboring microscopy room. The first measurement was acquired at ~3 minutes post-irradiation, which was the approximate time taken to locate the same cells measured before γ-irradiation. In the cases where the same cells could not be located within 3 minutes, these cells were discarded and another dish of cells was used. Subsequent measurements were acquired at about 5, 10, 15, 20, 30, 40 and 60 minutes post-irradiation. Ten cells were used for each time point with results being averaged from several experiments. For V3 cells the kinetics of YFP-DNA-PKcs were quantified for 1, 5, and 7 Gy. For Xrs6 cells the kinetics of GFP-Ku80 were quantified for 1, 5 and 10 Gy. The images acquired under these conditions were process by N&B analysis using commercially available software (Globals, Laboratory for Fluorescence Dynamics, Irvine, CA). During data analysis the photobleaching and cell movement effects were removed using a high-pass filter as described previously [10, 45]. The number of molecules per pixel estimated from Eq. 2.14 was then corrected for the presence of an immobile fraction, to arrive at the true number of mobile molecules per pixel (n_{mobile}) [48]:

$$n_{mobile} = n(1+R) + I_{immobile}\ (1+R)/\varepsilon \tag{5.1}$$

where *R* was the ratio between the intensity of immobile molecules to that of the mobile molecules per pixel. The *R* value was calculated from strip-FRAP analysis as the ratio of immobile to mobile fraction after fluorescence recovery reached a plateau after photobleaching as explained here below. Strip-FRAP measurements were performed on fresh cells, i.e. not the same cells that the N&B measurements were performed on and the deduced value of *R* was deduced as the average value from 10 cells measured for each cell line. Specifically, a strip of 80 x 10 pixels (0.1 μm pixel size) in the nucleus was selected from 128 by 128 pixels (13 μm by 13 μm) image and photobleached for 0.58 seconds using the 488 nm line of the Argon/2-laser at a power of ~0.55 mW at the focal spot for GFP-Ku80 cell and the 514 nm line from the same laser at ~420 mW for YFP-DNA-PKcs cells. For GFP-Ku80 the pre-bleach and post-bleach fluorescence within the strip were measured by taking continuous confocal images, from 5 seconds pre-bleach to 20 seconds post-bleach in 20 milliseconds time intervals. All other Strip-FRAP image acquisition settings on the LSM META 510 microscope for the two cell lines were identical to those used for confocal imaging, as described above. Fig. 5.2 below shows an example of how the immobile and immobile fraction of the protein was obtained from these Strip-FRAP measurements to calculate their ratio, *R*. This figure indicates the time independence (Fig. 5.2A) and the dose independence (Fig. 5.2B) for GFP-Ku80. Similar time and dose independence characteristics were also seen for γ-irradiation of YFP-DNA-PKcs and also for all bleomycin doses for both DNA repair proteins (data not shown for brevity). The R values found this way for the YFP-DNA-PKcs and GFP-Ku80 were 0.19 and 0.12, respectively.

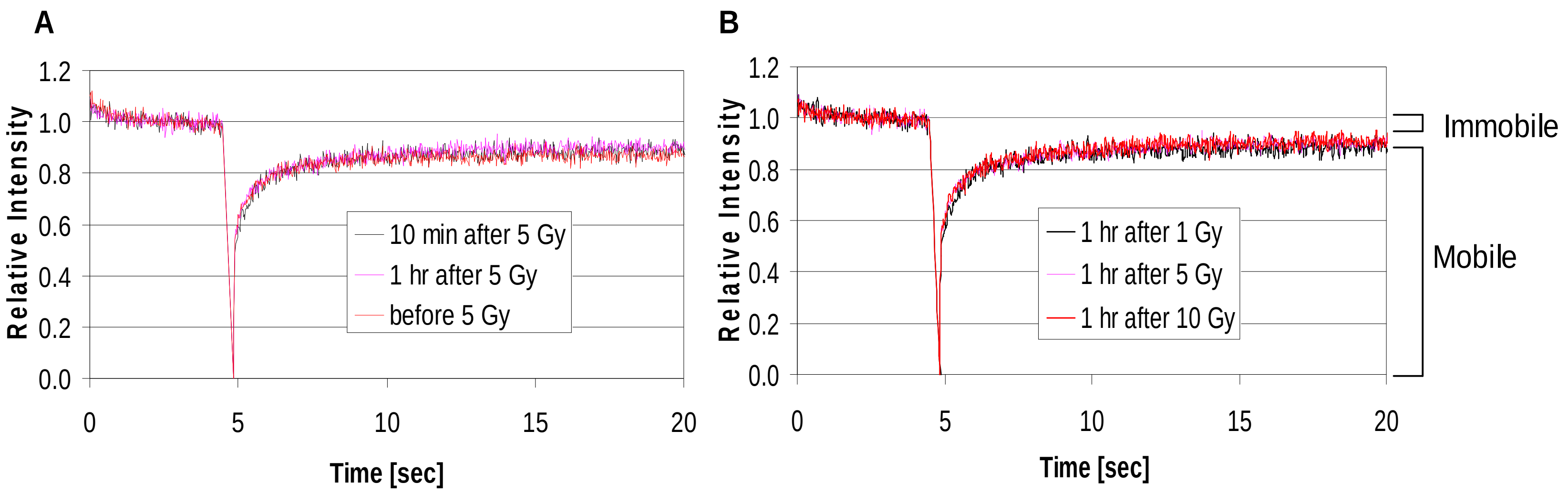

Fig. 5.2. Strip-FRAP measurements on Xrs6 cells expressing GFP-Ku80, (A) as a function of time before and after 5 Gy of γ-irradiation, and (B) as a function of dose at 1 hr post-irradiation. Data sets were normalized to pre-bleach values.

Once the *R* value was known, the normalized difference between the number of mobile molecules per pixel before and after irradiation, each calculated using Eq. 5.1, was used to calculate the bound fraction of molecules per pixel at each time point post-irradiation, as shown in Eq. 5.2:

$$n_r = \frac{(n_{mobile_i} - n_{mobile_o})}{(n_{mobile_o})} \tag{5.2}$$

where n_r was the relative bound fraction change, n_{mobile_o} the number of mobile molecules per pixel before irradiation, and n_{mobile_i} the number of mobile molecules per pixel at a particular time post-irradiation. The change of immobile fraction as a function of time post-irradiation is in fact the desired bound protein fraction that we have quantified in this work as a surrogate measure for quantifying the DNA repair for Ku70/80 and DNA-PKcs.

Similar to the γ-irradiation experiments, Eq. 5.2 was also used to quantify the relative bound fraction change for GFP-Ku80 and YFP-DNA-PKcs before exposure to bleomycin and at 5, 10, 15, 20, 30, 40 and 60 minutes post-treatment. It is important to note that for both γ-irradiation and bleomycin treatments ~30% of cells did not show any detectable kinetics for GFP-Ku80 or YFP-DNA-PKcs, presumably because the cells were in S-phase where DSB repair mechanisms are not predominant. Measurements for these cells were not included in any subsequent analyses.

5.2.6 Raster-scan Image correlation spectroscopy (RICS)

Spatio-temporal correlation images of RICS data were calculated with the Globals software package (Laboratory for Fluorescence Dynamics, Irvine, CA) that uses the RICS equation (Eq. 2.7) [9, 44]. The data obtained from the correlation images was then fitted to Eq. 2.8 which has two components, one due to correlation between neighboring pixel intensity values from particle diffusion, G_D (Eq. 2.9), and one due to correlation between neighboring pixel intensity values as a result of the beam raster scanning, G_S (Eq. 2.10). γ is a factor equal to 0.35 that accounts for the assumed 3D Gaussian profile of the confocal volume [9], and w_o,

w_z are the 1/e^2 beam waist values for the radial and axial directions, respectively, that were also used for FCS measurements.

For the RICS experiments stacks of images was acquired using the LSM 510 META microscope and ConfoCor3 attachment, similar to what described for the N&B analysis above. In contrast to N&B analysis, the selection of pixel size and scan speed are critical to measuring spatio-temporal correlations successfully [44, 45]. Both of these parameters depend on the molecular weight of the protein [45]. In this work a 256 pixels were used and pixel dwell time of 6.39 µs and 12.79 µs for GFP-Ku80 and YFP-DNA-PKcs, respectively. The pixel size was controlled by the electronic zoom which was set to 15 in order to fit a 256x256 pixel area within the FOV. This combination of spatio-temporal sampling settings resulted in frame rates of 0.98 seconds and 1.96 seconds for GFP-Ku80 and YFP-DNA-PKcs, respectively. Importantly, these sampling constraints restricted the FOV size to about 7 x 7 µm and 20 x 20 µm and therefore only one cell could be measured with RICS at a time.

It should be noted that an additional correlation component due to triplet state blinking [9] was not considered in this analysis because it occurred at shorter time scales than the protein kinetics being measured and was dealt with by removing the early correlation data, which was advantageous to fitting stability over having the triplet lifetime as an additional fitting component. It should also be mentioned that other existing RICS models including a second diffusion component or binding [44], which involved a higher number of fitting parameters, could not be supported by the data acquired in this work. RICS analysis was therefore limited to single component diffusion that yielded only an effective diffusion coefficient (D_{eff}) representing a population-averaged value of the mobility of proteins in the nucleus. A fraction of these proteins moved more slowly, with this fraction reducing with time post-damage as DNA repair progressed, while the remainder of repair proteins diffused freely. As a result, the value of D_{eff} was time-dependent.

A visual example of how the RICS data was processed is shown in Fig. 5.3. Once the cell to be measured was selected, a stack of images was acquired with the above described microscope settings (30 to 50 images, corresponding to measurement times of 59 to 98 seconds per time point). A region of interest, a clip box of 128 x 128 pixels (Fig. 5.3A) within the acquired 256 x 256 was cropped and the 2D spatio-temporal correlation function computed using Eq. 5.11 (Fig. 5.3B). Then the computed 2D autocorrelation surface (Fig. 5.3C) was fitted to the diffusion model of Eq. 5.12. A background correction was performed in order to remove stationary or slow moving objects and this is achieved by subtracting each pixel of an image from the average of all pixels [111].

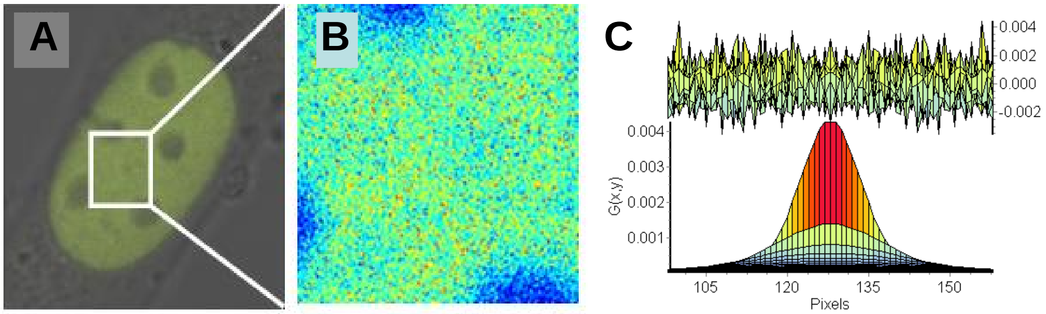

Figure 5.3 (A) Merge of confocal and DIC images of a V3 cell expressing YFP-DNA-PKcs, with the inset showing a user-selected region of the nucleus selected for RICS analysis; (B) Snapshot of the fluorescence intensity fluctuations in a background-corrected image of the selected ROI on which RICS analysis will be applied; (C) Fitting of the 2D RICS data obtained from Eq. 5.11 to the model described in Eq. 5.12 (top panel shows the fit residuals).

5.2.7 Monitoring repair protein kinetics after laser microirradiation by N&B and RICS analysis

Damage foci were induced in cultured cells by microirradiation with a nitrogen laser (Spectra-Phycics, Newport Corporation, Santa Clara) at 365 nm with an output power of 7.2 mW. The output laser power was set at 80% of the maximum, which was the minimal dose required to induce detectable accumulation of YFP-DNA-PKcs and GFP-Ku80 in living cells. To create this level of DNA damage this corresponded to a power of ~ 7 μW at the focal spot. Once the DNA damage was induced, the fluorescence buildup due to accumulation of the fluorescently tagged repair proteins at the damage focus, and the subsequent fluorescence decay as DNA repair progressed, was quantified by confocal time-lapse imaging and use of the system software (Carl Zeiss MicroImaging, Inc.) for subsequent image analysis. The laser beam was focused to the sample by a Plan-Apochromat 63×/NA 1.40 oil immersion objective (Carl Zeiss MicroImaging, Inc.). During both microirradiation and imaging the cells were maintained at 37℃ in 35-mm glass-bottom culture dishes (MatTek Cultureware). The growth medium was replaced by CO_2- independent media (Invitrogen) before microirradiation and imaging.

Immediately after irradiating the nucleus of a cell by laser RICS data was acquired with the same scanning parameters and at the same post-damage points described above for γ-irradiation. The RICS analysis yielded D_{eff} values for ROIs including the laser damage hot spot and for ROIs at different distances away from it. The same data was also subjected to N&B analysis to deduce the relative change in mobile fraction (Eq. 5.2) at different distances from the damage hot spot as a function of time post-damage, with Strip-FRAP correction applied similar to what was described in Fig. 5.2 above for γ-irradiation.

5.2.8 Statistical analysis

The statistical significance of any differences in relative mobile fraction for GFP-Ku80 and YFP-DNA-PKcs after different γ-irradiation doses and the comparison of these curves with corresponding N&B analysis kinetics after laser damage, across the ensemble of time-points where measurements were performed, were tested by linear mixed model analysis [68]. For comparisons of diffusion coefficients between RICS and FCS the Student’s t-test was used with a value of $p < 0.05$ considered as the threshold of statistical significance. Because we measured the same variables for multiple time points on the same cells, a linear mixed model [68] had to be applied to take into account the possible correlation structure between the repeated measures.

5.3 Results and Discussion

5.3.1 Comparison of N&B and RICS analysis with FCS

FCS is a very dependable method to monitor kinetics of proteins in homogeneous solutions *in vitro*, but is more challenging to apply in living cells due to a large background of immobile or low-mobility protein that is often present [41]. The latter was indeed the case for the proteins studied in this work, which made repeated measurements by FCS in the same cell difficult due to photobleaching (Figs. 5.4A-E). The RICS and N&B methods are raster scanning techniques that incur less photobleaching as they spread their light dose over a larger area of the cell [9, 19]. We have indeed found this to be the case in this work as shown in Figs.5.4 F-J (bottom row) for RICS, where the percentage loss in intensity between the first and last time-point post-irradiation was 10% on average, whereas the fluorescence loss for FCS was much higher at the same time interval. These findings were similar for the N&B measurements performed in this work.

Before applying RICS to the quantification of repair protein kinetics, it was validated that there was agreement between the D values obtained by this method compared to FCS measurements on the same cells. Measurements were performed on 10 cells with each method. It was found that D_{eff} values obtained by RICS for GFP-Ku80 ($14.59 \pm 2.77\ \mu m^2/s$) and YFP-DNA-PKcs ($6.17 \pm 0.49\ \mu m^2/s$) were in agreement with the corresponding values obtained with the fast diffusion component of FCS ($13.95 \pm 1.77\ \mu m^2/s$ and $5.96 \pm 0.45\ \mu m^2/s$,

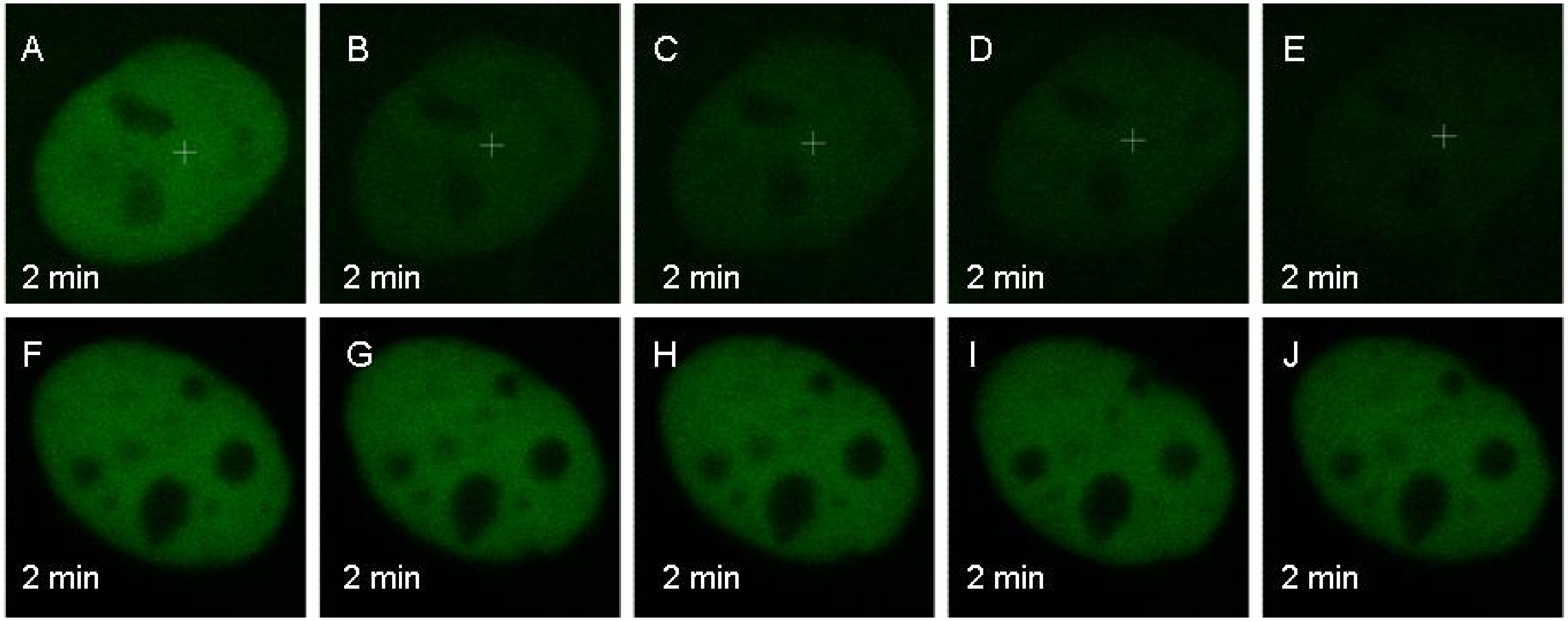

Figure 5.4 (A-E) Confocal images of an Xrs6 cell expressing GFP-Ku80 when consecutive point FCS measurements are performed and (F-J) when consecutive RICS experiments are performed.

respectively) with pair-wise differences between the two methods being non-statistically significant. On the other hand, no further validation was needed for N&B analysis in this work, beyond obtaining similar molecular N values for solutions of known fluorophore concentration (see Methods), as the DNA repair time-course measurements shown below are relative.

5.3.2 N&B and RICS analysis applied to the quantification of GFP-Ku80 repair kinetics after γ-irradiation

N&B analysis was first used to quantify changes in the mobile fraction of GFP-Ku80 as a function of time post-irradiation. Figure 5.5A shows the change in GFP-Ku80 mobile fraction after Xrs6 cells were treated with different doses (1, 5, 10 Gy) of γ-irradiation. The immobile fraction for these cells, as measured by strip-FRAP, was found to be ~10% both before and after γ-irradiation, irrespective of the dose used. It should also be noted that for each cell, the change in mobile fraction was normalized to the mobile fraction of the pre-irradiation time point so as to compensate for differences in protein expression levels between cells and thus be able to pull results from multiple cells. There was a dose-pendent low-level fluorescence loss post-irradiation that was noticed consistently in all measurements. We speculate that the fluorescence loss occurred as secondary damage resulting from the generation of free electron radicals during irradiation. However, for the case of GFP-Ku80 this loss was only a few percent. The level of fluorescence loss due to the irradiation was quantified by measuring 10 cells per dose at 4 hrs post irradiation where repair for most cells is known to be complete by that time point [22]. No measurements were performed at prior time points for these cells to avoid any further loss of fluorescence due to photobleaching from repeated N&B measurements. This loss factor was then subtracted from n_{mobile} in Eq. 5.2 above to yield a corrected value for this variable.

Subsequently, the relative mobile fraction change (Eq. 5.2) was normalized to unity at the time point with the maximum detected value which was ~5 min post-damage, i.e. at the shortest time possible for locating the same cluster of 3-4 cells post-irradiation. This type of normalization was used to show the dose independence in the GFP-Ku80 kinetics (Fig. 5.5A).

Linear mixed model analysis [68] indicated that the differences in mean relative change for dose were not significant (F(2,27)=3.06, p=.0.0636) this validating the expected dose independence of these kinetics. Also, just to help with visual interpretation of the data, a smooth log-normal function with four adjustable parameters was fitted through the different time points for each separate irradiation dose, using Sigma Plot (Systat Software, Inc, version 12).

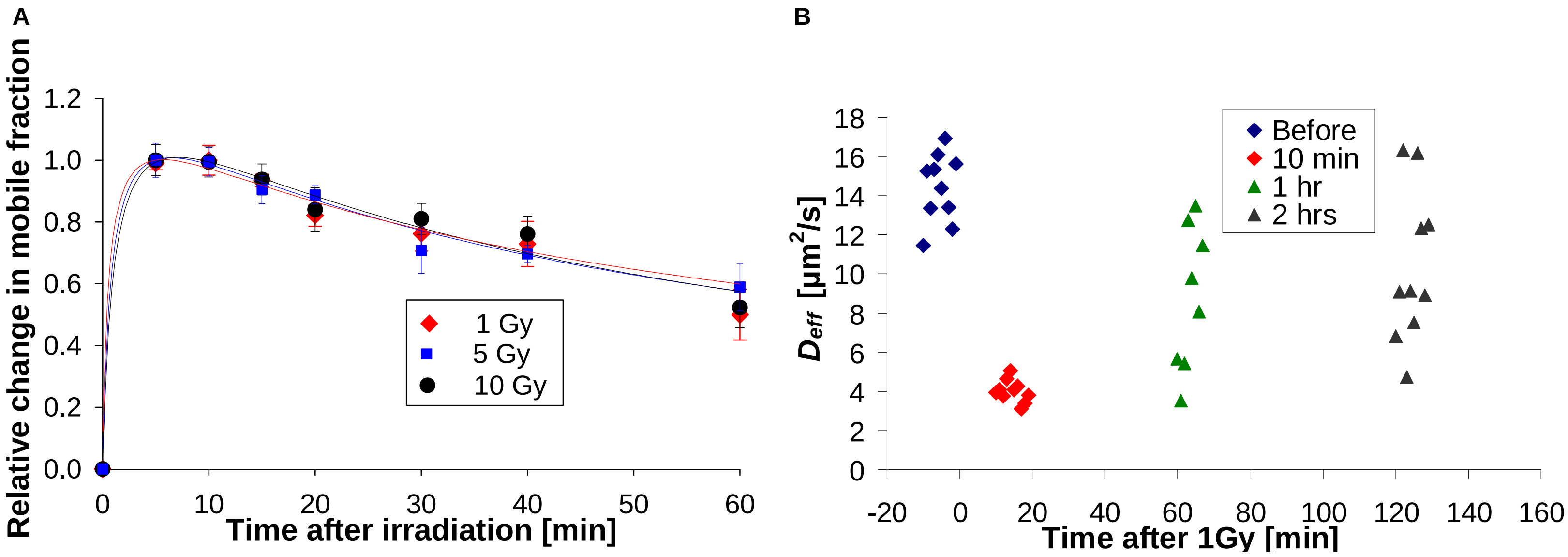

Figure 5.5 (A) Change in GFP-Ku80 relative mobile fraction as a function of time inside the nucleus of Xrs6 cells that were irradiated at different doses (1 Gy – diamonds, 5 Gy – squares, 10 Gy – circles). The error bars represent the standard error to the mean calculated from 10 different cells; (B) Variation of D_{eff} for GFP-Ku80 in Xrs6 cells; the average value was 14.42 ± 1.75 $\mu m^2/s$ before 1 Gy of γ-irradiation, 4.02 ± 0.57 $\mu m^2/s$ at 10 min, 8.77 ± 3.68 $\mu m^2/s$ at 1 hr and 10.36 ± 3.88 $\mu m^2/s$ at 2 hrs post-irradiation.

In addition to N&B analysis, the RICS method [9, 44] was also applied as an alternate approach to monitoring DNA repair kinetics after γ-irradiation. In RICS the change in D_{eff} of the fluorescently tagged repair protein was used as a surrogate measure of repair status, with complete repair being represented by a return of this diffusion coefficient to pre-irradiation values. For the case of GFP-Ku80 the change in D_{eff} was monitored at 10 min, 1 hr and 2 hrs after 1 Gy of γ-irradiation (Fig 5.5B). At 10 min post-irradiation all cells showed low D_{eff} values with little variation (4.02 ± 0.57 $\mu m^2/s$) compared to pre-irradiation values (14.42 ± 1.75 $\mu m^2/s$). However, with increasing time post-damage it was seen that some cells repair faster than others, as evidenced by the increasing spread in D_{eff} values at 1 hr (8.77 ± 3.68 $\mu m^2/s$) versus at 2 hrs (10.36 ± 3.88 $\mu m^2/s$), since there was not prior cell cycle synchronization performed. A linear mixed model with repeated measures was fitted to the diffusion data of Ku80 after gamma irradiation in order to ascertain whether there was any difference between mean diffusion at different times. The F-test (F(n,N); n= Degrees of Freedom; N= data points) was significant (F(3,27)=188.92, p<.0001) indicating that there was a difference between diffusion means between some time periods. Column three in Table 5.1 below shows the mean diffusion values for each time and table 5.2 below shows which of the pairs of means showed a significant difference and which did not.

Table 5.1 Least Square Means estimates of time effect for diffusion of Ku80 after treatment of γ-irradiation

Effect	Time[min]	Estimate ($\mu m^2/s$)	Standard Error
Time[min]	0	14.4192	0.5242
Time[min]	10	4.0184	0.1696
Time[min]	60	8.7699	0.9766
Time[min]	120	10.3599	1.1627

Table 5.2 Differences of Least Squares Means estimates of time effect for diffusion of Ku80 after treatment of γ-irradiation

Effect	Time[min]	Time[min]	Estimate	Standard Error	DF	t Value	Pr > |t|
Time[min]	0	10	10.4008	0.4419	27	23.53	<.0001
Time[min]	0	60	5.6493	1.0388	27	5.44	<.0001
Time[min]	0	120	4.0593	1.1588	27	3.5	0.0016
Time[min]	10	60	-4.7515	0.9739	27	-4.88	<.0001
Time[min]	10	120	-6.3416	1.2254	27	-5.18	<.0001
Time[min]	60	120	-1.59	1.7609	27	-0.9	0.3745

It should be noted that RICS data acquisition conditions required a small pixel size to capture spatio-temporal correlations of fluorescence, as described in the Methods above, which resulted in measuring the D_{eff} time course response for only one cell at a time. This requirement made RICS experiments much more time consuming than N&B ones, which are not as sensitive to pixel size and therefore enabled having 3-4 cells in the FOV at the same time. Nevertheless, the choice of larger pixel size in N&B for the sake of expedience came with a compromise: larger pixel sizes contain larger numbers of molecules that in turn reduce the amplitude of fluorescence fluctuations, which is the basis of the N&B signal (Eqs. 5.1 and 5.2). In this work, the mobile fraction at time points beyond 1 hr post-irradiation started becoming comparable to photobleaching corrected pre-irradiation values and, as a result, the change in mobile fraction was no longer detectable. Had the choice of pixel size been smaller, as was the case for RICS, the N&B analysis could have also been carried out to 2 hrs post-irradiation, but at the cost of measuring only one cell at a time.

5.3.3 N&B and RICS analysis applied to the quantification of YFP-DNA-PKcs repair kinetics after γ-irradiation

N&B measurements were also performed to quantify the repair kinetics of YFP-DNA-PKcs in V3 cells after γ-irradiation at experimental conditions very similar to the ones described above for GFP-Ku80. The only difference was that the highest dose used was 7 Gy and not 10 Gy. This was necessitated by the increased sensitivity of the YFP-tagged protein to loss of fluorescence after γ-irradiation compared to that of the GFP-tagged one. The reason for this is unclear. Despite these does-dependent losses of fluorescence, there was enough fluorescence signal post-irradiation to enable quantification of repair kinetics once this loss factor was compensated for in Eq. 5.2, as was done for GFP-Ku80 above. Fig. 5.6A shows the dose-independence of the YFP-DNA-PKcs kinetics. A linear mixed model with repeated measures was fitted to the DNA-PKcs kinetics data to determine whether there was a difference in mean relative change between the different dose levels. The model fitted relative change as a function of dose, time [minutes], and dose by time[minutes] interaction. The dose by time [minutes] interaction was not significant (F(14,189)=0.58, p=.8801) indicating that the differences in mean relative change between doses were the same regardless of time and the differences in mean relative change between times was the same regardless of dose. The differences in mean relative change for dose was not significant (F(2,27)=0.63, p=.5381) indicating that there were no differences between mean relative change between doses. The time main effect was significant (F(7,189)=275.38, p<.0001) indicating that there was a difference in relative change among times. Table 5.3 shows the tests of fixed effects and table 5.4 shows the means for relative change per dose.

Table 5.3 Tests of Fixed Effects for kinetics of DNA PKcs after treatment of γ-irradiation

Effect	Num DF	Den DF	F Value	Pr > F
Dose	2	27	0.63	0.538
Time[min]	7	189	275.38	<0.0001
Dose* Time[min]	14	189	0.58	0.8801

Table 5.4 Least Square Means estimates of dose effect on kinetics of DNA-PKcs after treatment of γ-irradiation

Effect	Time[min]	Estimate	Standard Error
Dose	1	0.1555	0.01835
Dose	5	0.1530	0.01431
Dose	7	0.1367	0.01054

In addition, RICS measurements were performed for experimental conditions very similar to those described for GFP-Ku80 above. A similar overall pattern of increasingly returning towards pre-irradiation D_{eff} values was also seen in this case, with mean values decreasing to (3.35 ± 0.99 $\mu m^2/s$) compared to pre-irradiation values (6.17 ± 0.49 $\mu m^2/s$). The mean D_{eff} values at the 1 hr and 2 hr time points were 4.80 ±1.09 $\mu m^2/s$ and 5.39 ±1.23 $\mu m^2/s$, respectively, and had a wider spread with respect to pre-irradiation values, reflecting ongoing repair. Interestingly, the spread of D_{eff} values at early times post-irradiation was higher for YFP-DNA-PKcs compared to the corresponding GFP-Ku80 data seen in Fig. 5.6B. This observation is qualitatively consistent with the slightly earlier peak time and the somewhat steeper descending slope within the first 30 minutes seen in Fig. 5.6A, compared to the corresponding mobile fraction changes for GFP-Ku80 seen in Fig. 5.5A, which indicate faster kinetics for YFP-DNA-PKcs at this initial period. These observations are consistent with the known notion that Ku70/80 is the first molecule to arrive at a DSB and is necessary for the subsequent recruitment of DNA-PKcs at the damage site [22].

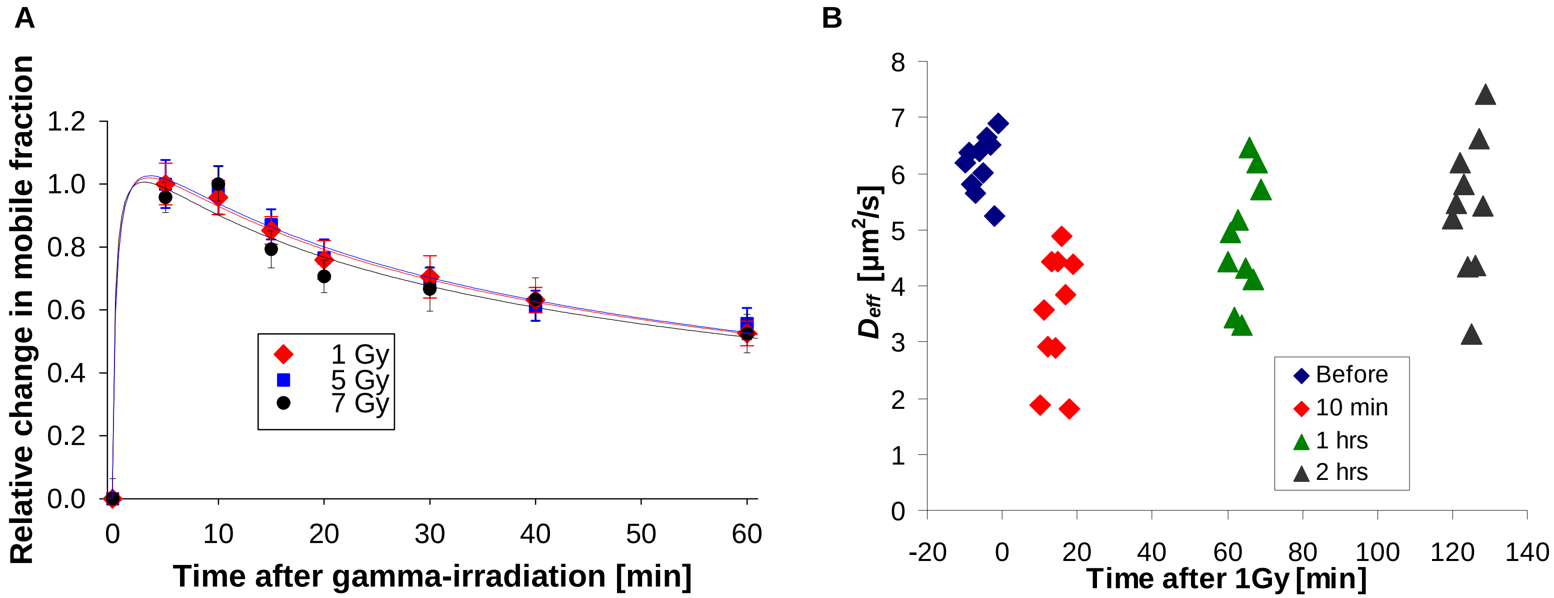

Figure 5.6 (A) Change in YFP-DNA-PKcs relative mobile fraction as a function of time post-irradiation for V3 cells irradiated at different doses (1 Gy – diamonds, 5 Gy – triangles, 7 Gy – filled squares) . The error bars represent the standard error to the mean calculated from 10 different cells; (B) Variation of D_{eff} for YFP-DNA-PKcs in V3 cells; the average value was 6.17 ± 0.49 μm^2/s before 1 Gy of γ-irradiation, 3.35 ± 1.08 μm^2/s at 10 min, 4.80 ±1.09 μm^2/s at 1 hr and and 5.39 ±1.23 μm^2/s at 2 hrs post-irradiation.

A linear mixed model with repeated measures was fitted to the DNA PKcs diffusion data after γ–irradiation to ascertain whether there was any difference between mean diffusion at different times. The F-test was significant (F(3,27)=33.34, p<.0001) indicating that there was a difference between diffusion means between some time periods. Table 5.5 shows the mean diffusion values for each time and table 5.6 shows which of the pairs of means showed a significant difference and which did not, indicating that it was primarily the differences with respect to pre-irradiation conditions and the first time point post-irradiation that were significant.

Table 5.5 Least Square Means estimates of time effect for diffusion of DNA-PKcs after treatment of γ-irradiation

Effect	Time[min]	Estimate	Standard Error
Time[min]	0	6.1688	0.1482
Time[min]	10	3.5021	0.3289
Time[min]	60	4.8080	0.3274
Time[min]	120	5.3945	0.3709

Table 5.6 Differences of Least Squares Means estimates of time effect for diffusion of DNA-PKcs after treatment of γ-irradiation

Effect	Time[min]	Time[min]	Estimate	Standard Error	DF	t Value	Pr > |t|
Time[min]	0	10	2.6667	0.2865	27	9.31	<.0001
Time[min]	0	60	1.3608	0.3591	27	3.79	0.0008
Time[min]	0	120	0.7743	0.3738	27	2.07	0.048
Time[min]	10	60	-1.3059	0.3999	27	-3.27	0.003
Time[min]	10	120	-1.8924	0.5056	27	-3.74	0.0009
Time[min]	60	120	-0.5865	0.4703	27	-1.25	0.2231

5.3.4 Validation experiments at inhibited repair conditions

Control experiments were performed to validate the expected reduction in mobile fraction change as a function of time post-irradiation under inhibited repair conditions for GFP-Ku80 and YFP-DNA-PKcs. Specifically, the repair kinetics of GFP-Ku80 were quantified after exposure to Wortmannin, a covalent inhibitor of phosphoinositide 3-kinases (PI3Ks) known to inhibit Ku70/80 [23](Fig. 5.7A). Also, the repair kinetics of the YFP-tagged 7A phosphorylation deficient mutant of DNA-PKcs were quantified after exposure to a dose of 1 Gy (Fig. 5.7B). Clear differences were seen for both GFP-Ku80 and YFP-DNA-PKcs with respect to the non-inhibited repair conditions as indicated by the persistence of a high bound fraction even at 1 hr post-irradiation. These findings are consistent with other reports in the literature for these two proteins [22]

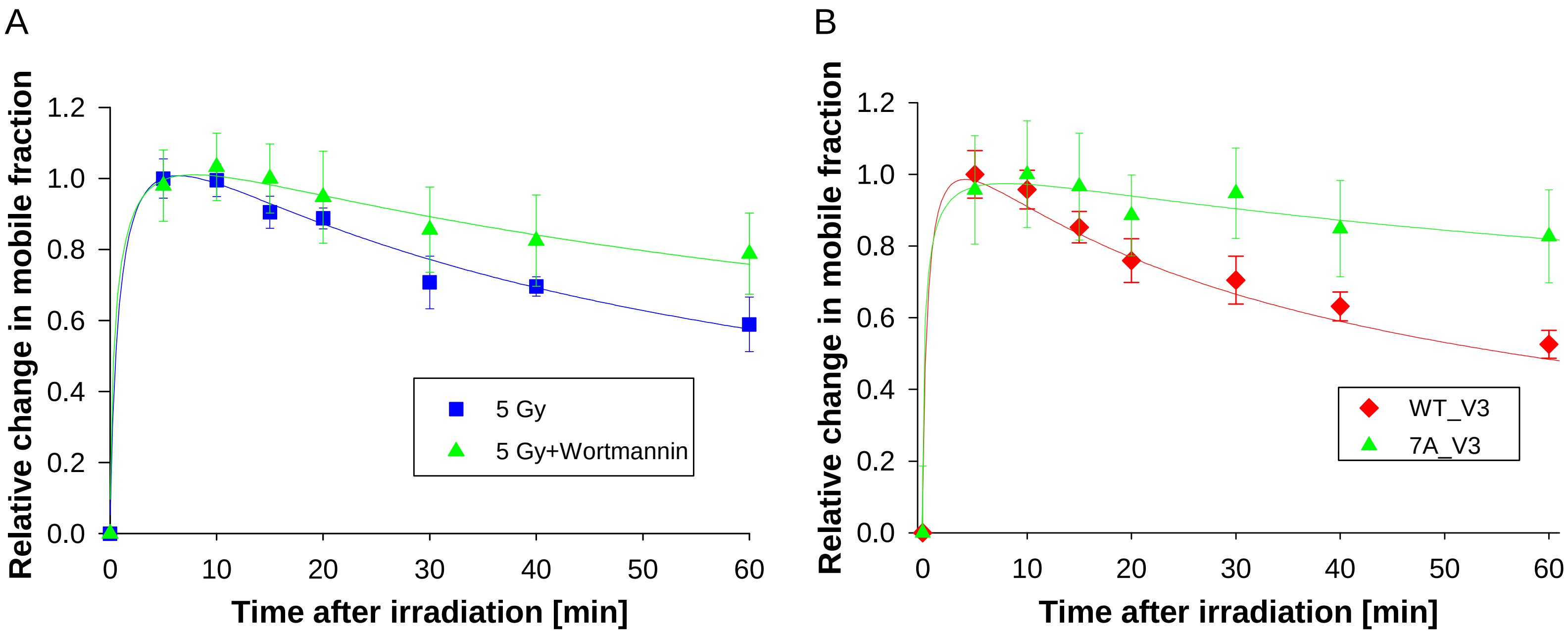

Figure 5.7 (A) Change in GFP-Ku80 relative mobile fraction as a function of time post-irradiation for Xrs6 cells irradiated with 5 Gy (filled squares) and for the same cells irradiated with the same dose after exposure to Wortmannin (triangles). The error bars represent the standard error to the mean calculated from 10 different cells; (B) Change in relative mobile fraction of wild type (WT) YFP-DNA-PKcs as a function of time post-irradiation for V3 cells irradiated with 1 Gy and corresponding kinetics for the 7A-DNA-PKcs phosphorylation mutant for the same dose.

5.3.5 Repair kinetics after bleomycin treatment

In addition to exposing the GFP-Ku80 and YFP-DNA-PKcs expressing cell lines to γ-irradiation the same cell lines were also exposed to bleomycin, a radiomimetic chemical that forms primarily DSBs [112-114]. The difference with respect to γ-irradiation was that DNA damage continued to occur even after the chemical was washed out of the cell media. This is because some of the chemical was already inside the cell and could not be removed by washing. As a result the kinetics observed for bleomycin represented a convolution of repair responses to DNA damage that occurred continuously, though ever less so with increasing time post-washing as the drug was turned over and excreted from the cell. Fig. 5.8A shows the kinetics for GFP-Ku80 for two different bleomycin doses (25 and 100 μg/ml). Interestingly, the lower of the two doses shows faster repair kinetics, while the two higher doses show slower kinetics, as DNA damage creation and chemical turnover persisted for longer. Also, in Fig. 5.8A it is seen that error bars were larger compared to the γ-irradiation experiments. We surmise that this is because of the greater variability in repair kinetics between cells as bleomycin uptake and turnover was an additional variable that was not present in the irradiation experiments. Due to these larger error bars it was not possible to distinguish statistically the 50 μg/ml from the 100 μg/ml data and only one smooth curve was fitted through both data sets in Fig. 5.8A. Similar observations were made for the YFP-DNA-PKcs, though the overall kinetics were rather slower after exposure to the same doses of bleomycin (Fig. 5.8B).

As was also seen in the γ-irradiation experiments, RICS analysis presented patterns of time-dependent changes in D_{eff} values after bleomycin treatment, with a heterogeneous increase towards pre-treatment values with time both for GFP-Ku80 (Fig.5.8C) and YFP-DNA-PKcs (Fig. 5.8D). Interestingly, a comparatively increased spread of D_{eff} values was seen at about 10-min post-treatment for YFP-DNA-PKcs compared to GFP-Ku80 implying faster repair kinetics, similar to corresponding observations in Fig. 5.7B versus Fig. 5.6B for γ-irradiation.

Such differences in repair kinetics were masked in the relative mobile fraction change plots, possibly due to differences in the chemical uptake and turnover between the two cell lines.

A linear mixed model with repeated measures was fitted to the diffusion data of DNA PKcs (Fig 5.8D) after bleomycin treatment to ascertain whether there was any difference between mean diffusion at different times. The F-test was significant (F(3,27)=15.59, p<.0001) indicating that there was a difference between diffusion means between some time periods. Table 5.7 shows the mean diffusion values for each time and table 5.8 shows which of the pairs of means showed a significant difference and which ones did not.

Table 5.7 Least Square Means estimates of time effect for diffusion of DNA-PKcs after bleomycin treatment

Effect	Time[min]	Estimate	Standard Error
Time[min]	0	6.1303	0.3573
Time[min]	10	3.1273	0.2329
Time[min]	60	4.6390	0.4212
Time[min]	120	5.4131	0.5132

Table 5.8 Differences of Least Squares Means estimates of time effect for diffusion of DNA-PKcs after bleomycin treatment

Effect	Time[min]	Time[min]	Estimate	Standard Error	DF	t Value	Pr > |t|
Time[min]	0	10	3.0029	0.4813	27	6.24	<.0001
Time[min]	0	60	1.4913	0.5352	27	2.79	0.0096
Time[min]	0	120	0.7172	0.6161	27	1.16	0.2546
Time[min]	10	60	-1.5117	0.4121	27	-3.67	0.0011
Time[min]	10	120	-2.2858	0.6321	27	-3.62	0.0012
Time[min]	60	120	-0.7741	0.8236	27	-0.94	0.3556

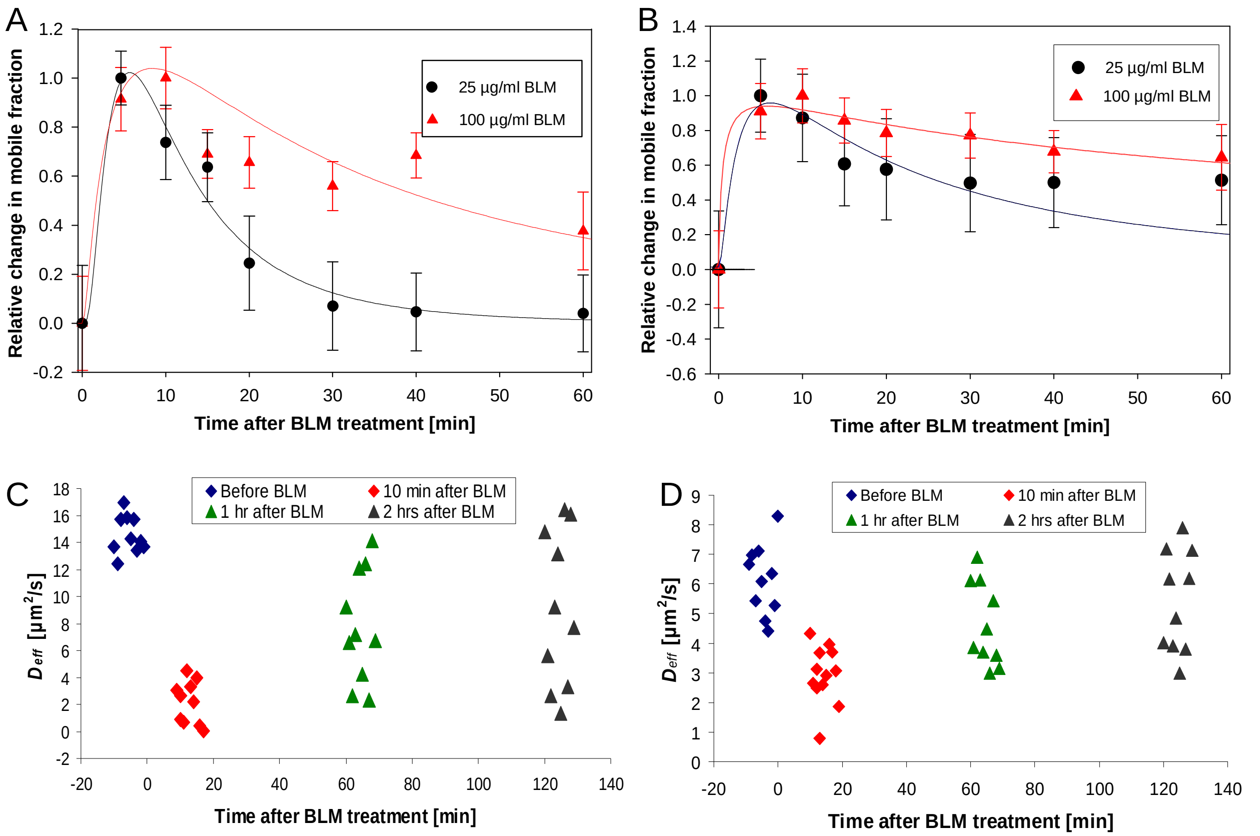

Figure 5.8 (A) Change in GFP-Ku80 relative mobile fraction as a function of time inside the nucleus of Xrs6 cells that were treated with different bleomycin doses (25 µg/ml – circles, 100 µg/ml – triangles); (B) Change in YFP-DNA-PKcs relative mobile fraction as a function of time inside the nucleus of V3 cells that were treated with different bleomycin doses (25 µg/ml – circles, 100 µg/ml – triangles). The error bars in both top panels represent the standard error to the mean calculated from 10 different cells; (C) Variation of D_{eff} for GFP-Ku80 as a function of time after bleomycin treatment; the average value was 14.57 ± 1.41 $\mu m^2/s$ before treatment, 2.17 ± 1.58 $\mu m^2/s$ at 10 min, 7.75 ± 4.35 $\mu m^2/s$ at 1 hr and 9.02 ± 5.78 $\mu m^2/s$ at 2 hrs post-treatment. (D) Variation of D_{eff} for YFP-DNA-PKcs as a function of time after bleomycin treatment; the average value was 6.13 ± 1.19 $\mu m^2/s$ before bleomycin treatment, 3.13 ± 0.78 $\mu m^2/s$ at 10 min, 4.64 ± 1.38 $\mu m^2/s$ at 1 hr and 5.41 ± 1.71 $\mu m^2/s$ at 2 hrs post-treatment.

A linear mixed model with repeated measures was fitted to the diffusion data of Ku80 (Fig 5.8C) after bleomycin treatment to ascertain whether there was any difference between mean diffusion at different times. The F-test was significant (F(3,27)=101.03, p<.0001) indicating that there was a difference between diffusion means between some time periods. Table 5.9 below shows the mean diffusion values for each time and table 5.10 below shows which of the pairs of means showed a significant difference.

Table 5.9 Least Square Means estimates of time effect for diffusion of Ku80 bleomycin treatment

Effect	Time[min]	Estimate	Standard Error
Time[min]	0	14.5754	0.4240
Time[min]	10	2.1678	0.4733
Time[min]	60	7.7530	1.2422
Time[min]	120	9.0201	1.7339

Table 5.10 Differences of Least Squares Means estimates of time effect for diffusion of Ku80 after bleomycin treatment

Effect	Time[min]	Time[min]	Estimate	Standard Error	DF	t Value	Pr > |t|
Time[min]	0	10	12.4077	0.7262	27	17.09	<.0001
Time[min]	0	60	6.8224	1.3819	27	4.94	<.0001
Time[min]	0	120	5.5553	1.8405	27	3.02	0.0055
Time[min]	10	60	-5.5853	1.4036	27	-3.98	0.0005
Time[min]	10	120	-6.8524	1.9339	27	-3.54	0.0015
Time[min]	60	120	-1.2671	0.7158	27	-1.77	0.088

CHAPTER 6

CONCLUSION

The standard method of studying DNA repair protein kinetics to date has been the use of laser microirradiation combined with time-lapse fluorescence microscopy, to follow the time-dependent intensity changes of a readily visible hot spot of fluorescently tagged proteins accumulating in an area of dense DNA damage [22]. This work demonstrates the feasibility of applying N&B and RICS analysis methods to study DNA repair kinetics after sparse DNA damage has occurred, which resembles more closely the type of damage occurring in cells after a therapeutic intervention. N&B and RICS were used in combination with strip-FRAP, to quantify changes in kinetics for two fluorescently tagged key NHEJ DNA repair pathway proteins, GFP-Ku80 and YFP-DNA-PKcs, after DSBs were induced by exposure to γ-irradiation or after exposure the radiomimetic chemical bleomycin.

The known dose independence of these two DNA repair proteins was validated for different γ-ray doses and also control experiments were performed where the function of these proteins was inhibited. The results obtained by N&B analysis both for baseline and repair-inhibited conditions were found to be consistent with corresponding laser microirradiation induced kinetics that were reported previously[23] Also, N&B analysis was used to quantify dose-dependent kinetics for GFP-Ku80 and YFP-DNA-PKcs after exposure to bleomycin. To our knowledge, this is the first time that the feasibility of quantifying repair kinetics after exposure to a radiomimetic chemical was shown for proteins that do not bind to DSBs in large numbers.

In addition to N&B analysis RICS measurements were performed to quantify an effective diffusion coefficient with time post-damage as an alternate surrogate measure of repair status. Comparisons of D_{eff} values after γ-irradiation and exposure to bleomycin suggested a faster disengagement of YFP-DNA-PKcs relative to GFP-Ku80 at early times post-damage. This trend was consistent with early repair kinetics observed by N&B analysis after γ-irradiation, but was masked in the N&B bleomycin experiments by variations in chemical uptake and turnover. Therefore in the latter case the RICS method appeared to be more informative.

Finally, since both N&B analysis and RICS could quantify molecular concentration, some consideration was given to the number and spatial distribution of repair proteins that become less mobile after DNA damage. It was interesting to find that a large number of proteins changed mobility per DSB and that these proteins had a gradient as a function of distance away from a damage hot spot, which suggested the existence of a mechanism of repair protein sequestration in the vicinity of DSBs.

The results of this work suggest the possible applicability of N&B and RICS analysis to the study of kinetics for numerous other DNA repair and signaling proteins that do not bind to DSBs in large numbers. Furthermore, combination of these methods with two-photon microscopy, which would enable greater penetration depth in tissues, could enable in the future the study of DNA repair under conditions that resemble the radiation therapy or chemotherapy of cancer.

APPENDIX A

LIST OF ABBREVIATIONS

AOM	acousto-optic modulator
APD	avalanche photodiode
ATM	ataxia telangiectasia mutated
ATR	ATM-Rad3 related
BER	base-excision repair
BLM	bleomycin
CCD	charge-coupled device
CLSM	confocal laser scanning microscope
CW	continuous wave
DNA	Deoxyribonucleic acid
DNA-PKcs	DNA-dependent protein kinase catalytic subunit
D_{eff}	effective diffusion
DSBs	DNA double-strand breaks
DsRed	red fluorescent protein
dsDNA	double strand DNA
EGFR	endothelial growth factor receptor
FCCS	fluorescence cross-correlation spectroscopy
FCS	fluorescence correlation spectroscopy
FRAP	fluorescence recovery after photobleaching
FOV	field of view
FS	Frame size (micrometer)
FSp	Frame size (in pixels)
FWHM	full width at half maximum
GFP	green fluorescent protein
HR	homologous recombination
ICS	image correlation spectroscopy

ICCS	image cross-correlation spectroscopy
kICS	k-space ICS
LSM	laser scanning microscope
LT	Line Time
NA	numerical aperture
NER	nucleotide-excision repair
NHEJ	non-homologous end-joining
N&B	number and brightness
PI-3-K	phosphatidylinositol-3-kinase
PIKK	phosphatidylinositol-3-kinase (PI-3-K)-related kinase
PSF	point-spread function
PT	Pixel Time
RF	relative fluorescence intensity
Rh6G	rhodamine 6G
RICS	raster-scan image correlation spectroscopy
ROI	region of interest
ROS	reactive oxygen species
RT	Retracting Time
SS	Scan Speed
SSA	single-strand annealing
ST	Scan Time
STICS	spatiotemporal-ICS
Strip-FRAP	Strip-fluorescence recovery after photobleaching
TICS	temporal-ICS
TNF	tumor necrosis factor
WT	wild type

XLF	XRCC4-like factor
XRCC4	X-ray cross complementing 4
YFP	yellow fluorescent protein

.

APPENDIX B

SCANNING PARAMETERS

Table B.1 Scanning parameters values for (C-Apochromat 40x/1.2 W corr) objective

						Z 5		**Z 10**		**Z 20**		**Z 30**		**Z 40**	
SS	PT [µs]	FSp [pixel]	ST [s]	RT [ms]	LT+RT [ms]	FS [µm]	PS [µm]	FS [µm]	PS [µm]	FS [µm]	PS [µm]	FS [µm]	PS [µm]	FS [µm]	PS [µm]
1	655.32	128	11.9	9.08	92.96	45	0.35	22.5	0.18	11.3	0.09	7.5	0.06	5.63	0.04
2	409.58	128	7.86	9.05	61.48	45	0.35	22.5	0.18	11.3	0.09	7.5	0.06	5.63	0.04
3	204.79	128	4.51	9.09	35.31	45	0.35	22.5	0.18	11.3	0.09	7.5	0.06	5.63	0.04
4	102.42	128	2.83	9.07	22.18	45	0.35	22.5	0.18	11.3	0.09	7.5	0.06	5.63	0.04
5	51.21	128	1.97	8.91	15.46	45	0.35	22.5	0.18	11.3	0.09	7.5	0.06	5.63	0.04
6	25.58	128	0.98	4.43	7.71	45	0.35	22.5	0.18	11.3	0.09	7.5	0.06	5.63	0.04
7	12.79	128	0.49	2.22	3.85	45	0.35	22.5	0.18	11.3	0.09	7.5	0.06	5.63	0.04
8	10.24	128	0.39	1.78	3.09	45	0.35	22.5	0.18	11.3	0.09	7.5	0.06	5.63	0.04
9	6.42	128	0.25	1.11	1.93	45	0.35	22.5	0.18	11.3	0.09	7.5	0.06	5.63	0.04
10	5.09	128	0.20	0.88	1.53	45	0.35	22.5	0.18	11.3	0.09	7.5	0.06	5.63	0.04
11	3.82	128	0.15	0.66	1.15	45	0.35	22.5	0.18	11.3	0.09	7.5	0.06	5.63	0.04
12	3.21	128	0.12	0.56	0.97	45	0.35	22.5	0.18	11.3	0.09	7.5	0.06	5.63	0.04
						45									
1	327.66	256	23.8	9.04	92.93	45	0.18	22.5	0.09	11.3	0.04	7.5	0.03	5.63	0.02
2	204.79	256	15.7	9.05	61.48	45	0.18	22.5	0.09	11.3	0.04	7.5	0.03	5.63	0.02

Table B.1 - *Continued*

3	102.39	256	9.02	9.06	35.27	45	0.18	22.5	0.09	11.3	0.04	7.5	0.03	5.63	0.02
4	51.21	256	5.66	9.03	22.14	45	0.18	22.5	0.09	11.3	0.04	7.5	0.03	5.63	0.02
5	25.61	256	3.93	8.83	15.39	45	0.18	22.5	0.09	11.3	0.04	7.5	0.03	5.63	0.02
6	12.79	256	1.96	4.40	7.67	45	0.18	22.5	0.09	11.3	0.04	7.5	0.03	5.63	0.02
7	6.39	256	0.98	2.21	3.84	45	0.18	22.5	0.09	11.3	0.04	7.5	0.03	5.63	0.02
8	5.12	256	0.79	1.77	3.08	45	0.18	22.5	0.09	11.3	0.04	7.5	0.03	5.63	0.02
9	3.21	256	0.49	1.11	1.93	45	0.18	22.5	0.09	11.3	0.04	7.5	0.03	5.63	0.02
1	163.83	512	47.6	9.03	92.91	45	0.09	22.5	0.04	11.3	0.02	7.5	0.01	5.63	0.01
2	102.39	512	31.5	9.02	61.44	45	0.09	22.5	0.04	11.3	0.02	7.5	0.01	5.63	0.01
3	51.20	512	18.0	9.02	35.23	45	0.09	22.5	0.04	11.3	0.02	7.5	0.01	5.63	0.01
4	25.61	512	11.3	9.03	22.15	45	0.09	22.5	0.04	11.3	0.02	7.5	0.01	5.63	0.01
5	12.80	512	7.87	8.83	15.39	45	0.09	22.5	0.04	11.3	0.02	7.5	0.01	5.63	0.01
6	6.39	512	3.93	4.41	7.68	45	0.09	22.5	0.04	11.3	0.02	7.5	0.01	5.63	0.01
7	3.20	512	1.96	2.19	3.83	45	0.09	22.5	0.04	11.3	0.02	7.5	0.01	5.63	0.01

Table B.1 - *Continued*

8	2.56	512	1.57	1.76	3.07	45	0.09	22.5	0.04	11.3	0.02	7.5	0.01	5.63	0.01
9	1.61	512	0.99	1.11	1.93	45	0.09	22.5	0.04	11.3	0.02	7.5	0.01	5.63	0.01
10	1.27	512	0.78	0.88	1.53	45	0.09	22.5	0.04	11.3	0.02	7.5	0.01	5.63	0.01

SS	Scan speed	**ST[s]**	Scan Time [s]	**FS [µm]**	Frame size [µm]
PT[µs]	Pixel Time [µs]	**RT[ms]**	Retracting Time [ms]	🟥	Under sampling
FSp[pixel]	Frame size [pixel]	**LT+RT[ms]**	Line time+retracing time [ms]	🟩	Over sampling

Table B.2 Scanning parameters values for Plan-Apochromat (63x/ 1.4 Oil Ph3) objective

						Z 5		Z 10		Z 20		Z 30		Z 40	
SS	PT [us]	FSp [pixel]	ST [s]	RT [ms]	LT+RT [ms]	FS [um]	PS [um]	FS [um]	PS [um]	FS [um]	PS [um]	FS [um]	PS [um]	FS [um]	PS [um]
1	655.32	128	11.89	9.08	92.96	28.57	0.22	14.3	0.11	7.14	0.06	4.76	0.04	3.57	0.03
2	409.58	128	7.86	9.05	61.48	28.57	0.22	14.3	0.11	7.14	0.06	4.76	0.04	3.57	0.03
3	204.79	128	4.51	9.09	35.31	28.57	0.22	14.3	0.11	7.14	0.06	4.76	0.04	3.57	0.03
4	102.42	128	2.83	9.07	22.18	28.57	0.22	14.3	0.11	7.14	0.06	4.76	0.04	3.57	0.03
5	51.21	128	1.97	8.91	15.46	28.57	0.22	14.3	0.11	7.14	0.06	4.76	0.04	3.57	0.03
6	25.58	128	0.98	4.43	7.71	28.57	0.22	14.3	0.11	7.14	0.06	4.76	0.04	3.57	0.03
7	12.79	128	0.49	2.22	3.85	28.57	0.22	14.3	0.11	7.14	0.06	4.76	0.04	3.57	0.03
8	10.24	128	0.39	1.78	3.09	28.57	0.22	14.3	0.11	7.14	0.06	4.76	0.04	3.57	0.03
9	6.42	128	0.25	1.11	1.93	28.57	0.22	14.3	0.11	7.14	0.06	4.76	0.04	3.57	0.03
10	5.09	128	0.20	0.88	1.53	28.57	0.22	14.3	0.11	7.14	0.06	4.76	0.04	3.57	0.03
11	3.82	128	0.15	0.66	1.15	28.57	0.22	14.3	0.11	7.14	0.06	4.76	0.04	3.57	0.03
12	3.21	128	0.12	0.56	0.97	28.57	0.22	14.3	0.11	7.14	0.06	4.76	0.04	3.57	0.03
13	2.56	128	0.10	0.44	0.77	28.57	0.22	14.3	0.11	7.14	0.06	4.76	0.04	3.57	0.03
1	327.66	256	23.78	9.04	92.93	28.57	0.11	14.3	0.06	7.14	0.03	4.76	0.02	3.57	0.01
2	204.79	256	15.73	9.05	61.48	28.57	0.11	14.3	0.06	7.14	0.03	4.76	0.02	3.57	0.01

															0.01
3	102.39	256	9.02	9.06	35.27	28.57	0.11	14.3	0.06	7.14	0.03	4.76	0.02	3.57	
4	51.21	256	5.66	9.03	22.14	28.57	0.11	14.3	0.06	7.14	0.03	4.76	0.02	3.57	0.01
5	25.61	256	3.93	8.83	15.39	28.57	0.11	14.3	0.06	7.14	0.03	4.76	0.02	3.57	0.01
6	12.79	256	1.96	4.40	7.67	28.57	0.11	14.3	0.06	7.14	0.03	4.76	0.02	3.57	0.01
7	6.39	256	0.98	2.21	3.84	28.57	0.11	14.3	0.06	7.14	0.03	4.76	0.02	3.57	0.01
8	5.12	256	0.79	1.77	3.08	28.57	0.11	14.3	0.06	7.14	0.03	4.76	0.02	3.57	0.01
9	3.21	256	0.49	1.11	1.93	28.57	0.11	14.3	0.06	7.14	0.03	4.76	0.02	3.57	0.01
10	2.55	256	0.39	0.88	1.53	28.57	0.11	14.3	0.06	7.14	0.03	4.76	0.02	3.57	0.01
11	1.91	256	0.29	0.66	1.15	28.57	0.11	14.3	0.06	7.14	0.03	4.76	0.02	3.57	0.01
12	1.61	256	0.25	0.55	0.97	28.57	0.11	14.3	0.06	7.14	0.03	4.76	0.02	3.57	0.01
13	1.28	256	0.20	0.44	0.77	28.57	0.11	14.3	0.06	7.14	0.03	4.76	0.02	3.57	0.01
1	163.83	512	47.56	9.03	92.91	28.57	0.06	14.3	0.03	7.14	0.01	4.76	0.01	3.57	0.01
2	102.39	512	31.45	9.02	61.44	28.57	0.06	14.3	0.03	7.14	0.01	4.76	0.01	3.57	0.01
3	51.20	512	18.03	9.02	35.23	28.57	0.06	14.3	0.03	7.14	0.01	4.76	0.01	3.57	0.01
4	25.61	512	11.33	9.03	22.15	28.57	0.06	14.3	0.03	7.14	0.01	4.76	0.01	3.57	0.01
5	12.80	512	7.87	8.83	15.39	28.57	0.06	14.3	0.03	7.14	0.01	4.76	0.01	3.57	0.01
6	6.39	512	3.93	4.41	7.68	28.57	0.06	14.3	0.03	7.14	0.01	4.76	0.01	3.57	0.01

7	3.20	512	1.96	2.19	3.83	28.57	0.06	14.3	0.03	7.14	0.01	4.76	0.01	3.57	0.01
8	2.56	512	1.57	1.76	3.07	28.57	0.06	14.3	0.03	7.14	0.01	4.76	0.01	3.57	0.01
9	1.61	512	0.99	1.11	1.93	28.57	0.06	14.3	0.03	7.14	0.01	4.76	0.01	3.57	0.01
10	1.27	512	0.78	0.88	1.53	28.57	0.06	14.3	0.03	7.14	0.01	4.76	0.01	3.57	0.01
11	0.95	512	0.59	0.66	1.15	28.57	0.06	14.3	0.03	7.14	0.01	4.76	0.01	3.57	0.01
12	0.80	512	0.49	0.56	0.96	28.57	0.06	14.3	0.03	7.14	0.01	4.76	0.01	3.57	0.01
13	0.64	512	0.39	0.44	0.77	28.57	0.06	14.3	0.03	7.14	0.01	4.76	0.01	3.57	0.01

SS	Scan speed	**ST[s]**	Scan Time [sec]	**FS[um]**	Frame size [um]
PT[us]	Pixel Time [usec]	**RT[ms]**	Retracting Time [msec]	🟥	Under sampling
FSp[pixel]	Frame size [pixel]	**LT+RT[ms]**	Line time + retracing time [msec]	🟩	Over sampling

APPENDIX C

PINHOLE ADJUSTMENT

Pinhole is first coarse adjusted in x direction to find the maximum intensity on x direction as shown in figure below. In order to adjust the pinhole, dye solutions are required. In this project Rhodamine 6G and Cy5 were mainly used.

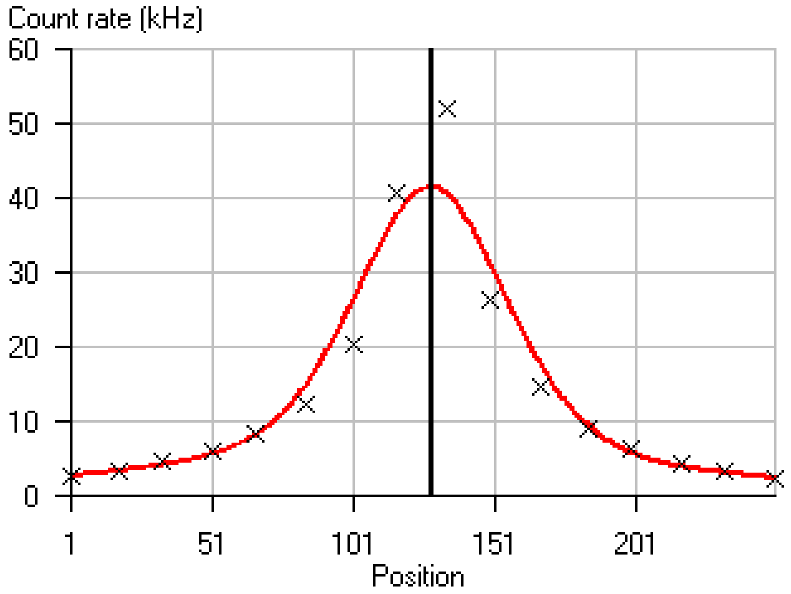

Then the pinhole is fine adjusted by scanning in x direction to find the maximum intensity on x direction as shown in figure below.

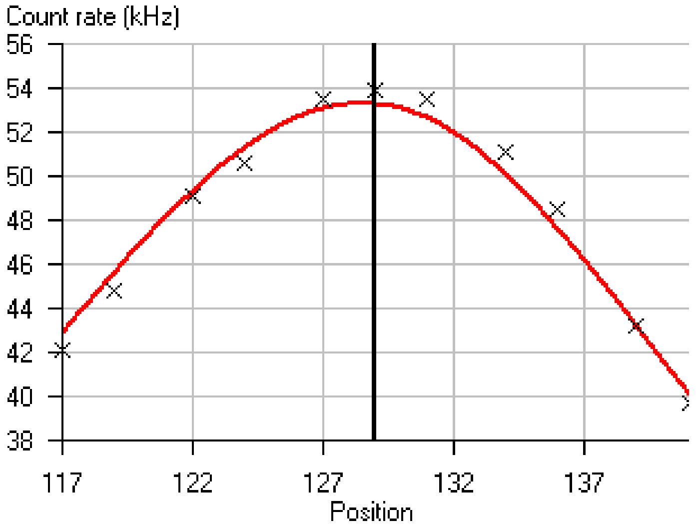

Then the coarse adjustment in y direction is performed to find the maximum intensity on y direction as shown in figure below.

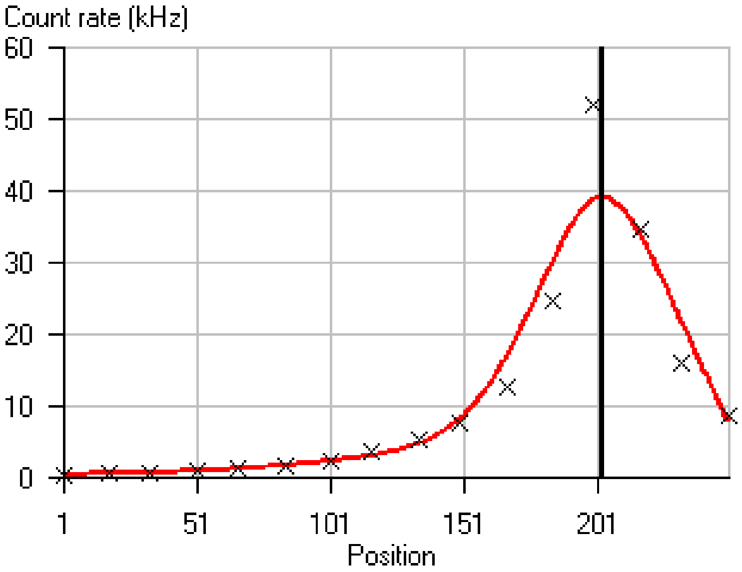

Pinhole is finally fine adjusted by scanning in y direction to find the maximum intensity on y direction as shown in figure below

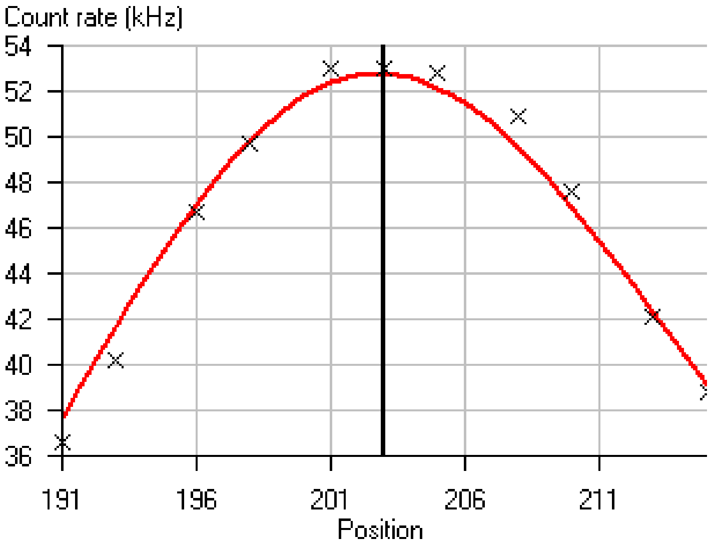

REFERENCES

1. Asaithamby, A. and D.J. Chen, *Cellular responses to DNA double-strand breaks after low-dose gamma-irradiation.* Nucleic Acids Res, 2009. **37**(12): p. 3912-23.
2. Ismail, I.H. and M.J. Hendzel, *The gamma-H2A.X: is it just a surrogate marker of double-strand breaks or much more?* Environ Mol Mutagen, 2008. **49**(1): p. 73-82.
3. Uematsu, N., et al., *Autophosphorylation of DNA-PKCS regulates its dynamics at DNA double-strand breaks.* J Cell Biol, 2007. **177**(2): p. 219-29.
4. Weterings, E. and D.C. van Gent, *The mechanism of non-homologous end-joining: a synopsis of synapsis.* DNA Repair (Amst), 2004. **3**(11): p. 1425-35.
5. Yano, K. and D.J. Chen, *Live cell imaging of XLF and XRCC4 reveals a novel view of protein assembly in the non-homologous end-joining pathway.* Cell Cycle, 2008. **7**(10): p. 1321-5.
6. Kong, X., et al., *Comparative analysis of different laser systems to study cellular responses to DNA damage in mammalian cells.* Nucleic Acids Res, 2009. **37**(9): p. e68.
7. Mahaney, B.L., K. Meek, and S.P. Lees-Miller, *Repair of ionizing radiation-induced DNA double-strand breaks by non-homologous end-joining.* Biochem J, 2009. **417**(3): p. 639-50.
8. Martensson, S., et al., *Activation of the DNA-dependent protein kinase by drug-induced and radiation-induced DNA strand breaks.* Radiat Res, 2003. **160**(3): p. 291-301.
9. Digman, M.A. and E. Gratton, *Analysis of diffusion and binding in cells using the RICS approach.* Microsc Res Tech, 2009. **72**(4): p. 323-32.
10. Digman, M.A., et al., *Stoichiometry of molecular complexes at adhesions in living cells.* Proc Natl Acad Sci U S A, 2009. **106**(7): p. 2170-2175.
11. van Gent, D.C., J.H. Hoeijmakers, and R. Kanaar, *Chromosomal stability and the DNA double-stranded break connection.* Nat Rev Genet, 2001. **2**(3): p. 196-206.
12. Miller, K.M., et al., *Human HDAC1 and HDAC2 function in the DNA-damage response to promote DNA nonhomologous end-joining.* Nature Structural & Molecular Biology, 2010. **17**(9): p. 1144-U15.
13. Chan, D.W., et al., *Purification and characterization of the double-stranded DNA-activated protein kinase, DNA-PK, from human placenta.* Biochemistry and Cell Biology-Biochimie Et Biologie Cellulaire, 1996. **74**(1): p. 67-73.
14. Abraham, R.T., *PI 3-kinase related kinases: 'big' players in stress-induced signaling pathways.* DNA Repair, 2004. **3**(8-9): p. 883-887.

15. Mari, P.O., et al., *Dynamic assembly of end-joining complexes requires interaction between Ku70/80 and XRCC4.* Proc Natl Acad Sci U S A, 2006. **103**(49): p. 18597-602.

16. Watson, N.B., et al., *RAD18 and associated proteins are immobilized in nuclear foci in human cells entering S-phase with ultraviolet light-induced damage.* Mutat Res, 2008. **648**(1-2): p. 23-31.

17. Abdisalaam, S.A., D.J. Chen, and G. Alexandrakis. *Raster Image Correlation Spectroscopy to Quantify DNA Repair Protein Kinetics*. in *SPIE - Photonics West*. 2011. San Fransisco, CA: SPIE.

18. Elson, E.L. and D. Magde, *Fluorescence Correlation Spectroscopy .1. Conceptual Basis and Theory.* Biopolymers, 1974. **13**(1): p. 1-27.

19. Digman, M.A., et al., *Mapping the number of molecules and brightness in the laser scanning microscope.* Biophys J, 2008. **94**(6): p. 2320-32.

20. Pramanik, A. and R. Rigler, *Ligand-receptor interactions in the membrane of cultured cells monitored by fluorescence correlation spectroscopy.* Biol Chem, 2001. **382**(3): p. 371-8.

21. Carl Zeiss MicroImaging, *Manual LSM 510 ConfCor 3. .* 2006 **Release 4.0**.

22. Uematsu, N., et al., *Autophosphorylation of DNA-PKCS regulates its dynamics at DNA double-strand breaks.* Journal of Cell Biology, 2007. **177**(2): p. 219-229.

23. Mari, P.O., et al., *Dynamic assembly of end-joining complexes requires interaction between Ku70/80 and XRCC4.* Proc Natl Acad Sci U S A, 2006. **103**(49): p. 18597-18602.

24. Davis, A.J., S. So, and D.J. Chen, *Dynamics of the PI3K-like protein kinase members ATM and DNA-PKcs at DNA double strand breaks.* Cell Cycle, 2010. **9**(13): p. 2529-2536.

25. So, S., A.J. Davis, and D.J. Chen, *Autophosphorylation at serine 1981 stabilizes ATM at DNA damage sites (vol 7, pg 977, 2009).* Journal of Cell Biology, 2010. **188**(3): p. 443-443.

26. Yano, K.I., et al., *Ku recruits XLF to DNA double-strand breaks.* Embo Reports, 2008. **9**(1): p. 91-96.

27. Reits, E.A.J. and J.J. Neefjes, *From fixed to FRAP: measuring protein mobility and activity in living cells.* Nature Cell Biology, 2001. **3**(6): p. E145-E147.

28. van Royen, M.E., et al., *Fluorescence recovery after photobleaching (FRAP) to study nuclear protein dynamics in living cells.* Methods Mol Biol, 2009. **464**: p. 363-85.

29. Phair, R.D., S.A. Gorski, and T. Misteli, *Measurement of dynamic protein binding to chromatin in vivo, using photobleaching microscopy.* Chromatin and Chromatin Remodeling Enzymes, Pt A, 2004. **375**: p. 393-414.

30. Vamosi, G., et al., *Measurement of molecular mobility with fluorescence correlation spectroscopy.* Curr Protoc Cytom, 2009. **Chapter 2**: p. Unit2 15.

31. Guo, L., et al., *Molecular diffusion measurement in lipid bilayers over wide concentration ranges: a comparative study.* Chemphyschem, 2008. **9**(5): p. 721-8.

32. Vukojevic, V., et al., *Study of molecular events in cells by fluorescence correlation spectroscopy.* Cell Mol Life Sci, 2005. **62**(5): p. 535-50.

33. Schwille, P., et al., *Fluorescence correlation spectroscopy reveals fast optical excitation-driven intramolecular dynamics of yellow fluorescent proteins.* Proc Natl Acad Sci U S A, 2000. **97**(1): p. 151-6.

34. Tian, Y., M.M. Martinez, and D. Pappas, *Fluorescence correlation spectroscopy: a review of biochemical and microfluidic applications.* Appl Spectrosc, 2011. **65**(4): p. 115A-124A.

35. Lamb, D.C., B.K. Muller, and C. Brauchle, *Enhancing the sensitivity of fluorescence correlation spectroscopy by using time-correlated single photon counting.* Current Pharmaceutical Biotechnology, 2005. **6**(5): p. 405-414.

36. Zhong ZH, P.A., Ekberg K, Jansson OT, Jörnvall H, Wahren J, Rigler R., *Insulin binding monitored by fluorescence correlation spectroscopy.* Diabetologia, 2001. **44**(9): p. 1184-8.

37. Pramanik A, R.R., *Ligand-receptor interactions in the membrane of cultured cells monitored by fluorescence correlation spectroscopy.* Biol Chem, 2001. **382**(3): p. 371-8.

38. van den Wildenberg, S.M.J.L., Y.J.M. Bollen, and E.J.G. Peterman, *How to Quantify Protein Diffusion in the Bacterial Membrane.* Biopolymers, 2011. **95**(5): p. 312-321.

39. Rigler, R., Pramanik, A., Jonasson, P., Kratz, G., Jansson, O.T., Nygren, P.-A., Stshl, S., Ekberg, K., Johansson, B.L., Uhlen, S., Uhlen, M., Jornvall, H. and Wahren, J. , *Specific binding of proinsulin C-peptide to human cell membranes.* Proc. Natl. Acad. Sci., 1999. **96**(23): p. 3318–13323.

40. Schwille, P., et al., *Molecular dynamics in living cells observed by fluorescence correlation spectroscopy with one- and two-photon excitation.* Biophys J, 1999. **77**(4): p. 2251-65.

41. Stasevich, T.J., et al., *Cross-validating FRAP and FCS to quantify the impact of photobleaching on in vivo binding estimates.* Biophys J, 2010. **99**(9): p. 3093-101.

42. Petersen, N.O., et al., *Quantitation of membrane receptor distributions by image correlation spectroscopy: concept and application.* Biophys J, 1993. **65**(3): p. 1135-46.

43. Kolin, D.L. and P.W. Wiseman, *Advances in image correlation spectroscopy: measuring number densities, aggregation states, and dynamics of fluorescently labeled macromolecules in cells.* Cell Biochem Biophys, 2007. **49**(3): p. 141-64.

44. Brown, C.M., et al., *Raster image correlation spectroscopy (RICS) for measuring fast protein dynamics and concentrations with a commercial laser scanning confocal microscope.* J Microsc, 2008. **229**(Pt 1): p. 78-91.

45. Digman, M.A., et al., *Measuring fast dynamics in solutions and cells with a laser scanning microscope.* Biophys J, 2005. **89**(2): p. 1317-27.

46. Digman, M.A., et al., *Paxillin dynamics measured during adhesion assembly and disassembly by correlation spectroscopy.* Biophys J, 2008. **94**(7): p. 2819-31.

47. Dalal, R.B., et al., *Determination of particle number and brightness using a laser scanning confocal microscope operating in the analog mode.* Microscopy Research and Technique, 2008. **71**(1): p. 69-81.

48. Ossato, G., et al., *A two-step path to inclusion formation of huntingtin peptides revealed by number and brightness analysis.* Biophys J, 2010. **98**(12): p. 3078-85.

49. Normanno, N., et al., *Epidermal growth factor receptor (EGFR) signaling in cancer.* Gene, 2006. **366**(1): p. 2-16.

50. Chen, D.J. and C.S. Nirodi, *The epidermal growth factor receptor: a role in repair of radiation-induced DNA damage.* Clin Cancer Res, 2007. **13**(22 Pt 1): p. 6555-60.

51. Chen, L.Q., et al., *Dual EGFR/HER2 Inhibition Sensitizes Prostate Cancer Cells to Androgen Withdrawal by Suppressing ErbB3.* Clinical Cancer Research, 2011. **17**(19): p. 6218-6228.

52. Olayioye, M.A., et al., *The ErbB signaling network: receptor heterodimerization in development and cancer.* EMBO J, 2000. **19**(13): p. 3159-67.

53. Hoffmann, M., M. Schmidt, and W. Wels, *Activation of EGF receptor family members suppresses the cytotoxic effects of tumor necrosis factor-alpha.* Cancer Immunol Immunother, 1998. **47**(3): p. 167-75.

54. Ciardiello, F. and G. Tortora, *Interactions between the epidermal growth factor receptor and type I protein kinase A: Biological significance and therapeutic implications.* Clinical Cancer Research, 1998. **4**(4): p. 821-828.

55. Szabo, A., J. Szollosi, and P. Nagy, *Coclustering of ErbB1 and ErbB2 revealed by FRET-sensitized acceptor bleaching.* Biophys J, 2010. **99**(1): p. 105-14.

56. Yarden, Y. and M.X. Sliwkowski, *Untangling the ErbB signalling network.* Nat Rev Mol Cell Biol, 2001. **2**(2): p. 127-37.

57. Chopra, A., *177Lu-Labeled h-R3 (nimotuzumab), a humanized monoclonal antibody targeting the external domain of the epidermal growth factor receptor.* 2004.

58. Bronte, G., et al., *EGFR genomic alterations in cancer: prognostic and predictive values.* Front Biosci (Elite Ed), 2011. **3**: p. 879-87.

59. Spitz, D.R., et al., *Metabolic oxidation/reduction reactions and cellular responses to ionizing radiation: a unifying concept in stress response biology.* Cancer metastasis reviews, 2004. **23**(3-4): p. 311-22.

60. Geoerger, B., et al., *EGFR tyrosine kinase inhibition radiosensitizes and induces apoptosis in malignant glioma and childhood ependymoma xenografts.* International Journal of Cancer, 2008. **123**(1): p. 209-216.

61. Wang, M., et al., *EGF receptor inhibition radiosensitizes NSCLC cells by inducing senescence in cells sustaining DNA double-strand breaks.* Cancer Res, 2011. **71**(19): p. 6261-9.

62. Contessa, J.N., et al., *ErbB receptor tyrosine kinase network inhibition radiosensitizes carcinoma cells.* Int J Radiat Oncol Biol Phys, 2006. **65**(3): p. 851-8.

63. Daly, C.J. and J.C. McGrath, *Fluorescent ligands, antibodies, and proteins for the study of receptors.* Pharmacology & Therapeutics, 2003. **100**(2): p. 101-118.

64. Dobbs, T.A., J.A. Tainer, and S.P. Lees-Miller, *A structural model for regulation of NHEJ by DNA-PKcs autophosphorylation.* DNA Repair (Amst), 2010. **9**(12): p. 1307-14.

65. Ossato, G., et al., *A Two-Step Path to Inclusion Formation of Huntingtin Peptides Revealed by Number and Brightness Analysis.* Biophysical Journal, 2010. **98**(12): p. 3078-3085.

66. Toulany, M., et al., *Blockage of epidermal growth factor receptor-phosphatidylinositol 3-kinase-AKT signaling increases radiosensitivity of K-RAS mutated human tumor cells in vitro by affecting DNA repair.* Clin Cancer Res, 2006. **12**(13): p. 4119-26.

67. Digman, M.A., et al., *Mapping the number of molecules and brightness in the laser scanning microscope.* Biophysical Journal, 2008. **94**(6): p. 2320-2332.

68. Muller, K.E.a.S., P.W., *Linear Model Theory: Univariate, Multivariate, and Mixed Models.* Wiley-Interscience, Hoboken, NJ, 2006.

69. Nakabeppu, Y., et al., *Biological significance of the defense mechanisms against oxidative damage in nucleic acids caused by reactive oxygen species: from mitochondria to nuclei.* Ann N Y Acad Sci, 2004. **1011**: p. 101-11.

70. Loft, S. and H.E. Poulsen, *Cancer risk and oxidative DNA damage in man.* J Mol Med (Berl), 1996. **74**(6): p. 297-312.

71. Franco, S., F.W. Alt, and J.P. Manis, *Pathways that suppress programmed DNA breaks from progressing to chromosomal breaks and translocations.* DNA Repair, 2006. **5**(9-10): p. 1030-1041.

72. Greenstock, C.L., *Radiation and aging: free radical damage, biological response and possible antioxidant intervention.* Med Hypotheses, 1993. **41**(5): p. 473-82.

73. Hoeijmakers, J.H., *Genome maintenance mechanisms for preventing cancer.* Nature, 2001. **411**(6835): p. 366-74.

74. Mao, X., et al., *Chromosome rearrangement associated inactivation of tumour suppressor genes in prostate cancer.* Am J Cancer Res, 2011. **1**(5): p. 604-17.

75. Weterings, E. and D.J. Chen, *The endless tale of non-homologous end-joining.* Cell Res, 2008. **18**(1): p. 114-24.

76. Ira, G., et al., *DNA end resection, homologous recombination and DNA damage checkpoint activation require CDK1.* Nature, 2004. **431**(7011): p. 1011-7.

77. Yun, M.H. and K. Hiom, *CtIP-BRCA1 modulates the choice of DNA double-strand-break repair pathway throughout the cell cycle.* Nature, 2009. **459**(7245): p. 460-3.

78. Chung, W.H., et al., *Defective Resection at DNA Double-Strand Breaks Leads to De Novo Telomere Formation and Enhances Gene Targeting.* Plos Genetics, 2010. **6**(5).

79. Hefferin, M.L. and A.E. Tomkinson, *Mechanism of DNA double-strand break repair by non-homologous end joining.* DNA Repair (Amst), 2005. **4**(6): p. 639-48.

80. Yano, K., et al., *Functional significance of the interaction with Ku in DNA double-strand break recognition of XLF.* FEBS Lett, 2011. **585**(6): p. 841-6.

81. Iliakis, G., et al., *Mechanisms of DNA double strand break repair and chromosome aberration formation.* Cytogenet Genome Res, 2004. **104**(1-4): p. 14-20.

82. Octobre, G., et al., *Monitoring the interaction between DNA and a transcription factor (MEF2A) using fluorescence correlation spectroscopy.* Comptes Rendus Biologies, 2005. **328**(12): p. 1033-1040.

83. Zhong, Z.H., et al., *Insulin binding monitored by fluorescence correlation spectroscopy.* Diabetologia, 2001. **44**(9): p. 1184-1188.

84. Pramanik, A. and R. Rigler, *Ligand-receptor interactions in the membrane of cultured cells monitored by fluorescence correlation spectroscopy.* Biological Chemistry, 2001. **382**(3): p. 371-378.

85. Zeiss, C., *Applications Manual for ConfoCor 3.* 2006(B 40-0015 e).

86. Schwille, P., et al., *Molecular dynamics in living cells observed by fluorescence correlation spectroscopy with one- and two-photon excitation.* Biophysical Journal, 1999. **77**(4): p. 2251-2265.

87. Rigler, R., et al., *Specific binding of proinsulin C-peptide to human cell membranes.* Proceedings of the National Academy of Sciences of the United States of America, 1999. **96**(23): p. 13318-13323.

88. Bacia, K. and P. Schwille, *A dynamic view of cellular processes by in vivo fluorescence auto- and cross-correlation spectroscopy.* Methods, 2003. **29**(1): p. 74-85.

89. Merkle, D., et al., *Analysis of DNA-dependent protein kinase-mediated DNA end joining by two-photon fluorescence cross-correlation spectroscopy.* Biochemistry, 2006. **45**(13): p. 4164-4172.

90. Bacia, K., S.A. Kim, and P. Schwille, *Fluorescence cross-correlation spectroscopy in living cells.* Nat Methods, 2006. **3**(2): p. 83-9.

91. Arosio, D., et al., *Studies on the mode of Ku interaction with DNA.* J Biol Chem, 2002. **277**(12): p. 9741-8.

92. Arosio, D., et al., *Fluorescence anisotropy studies on the Ku-DNA interaction: anion and cation effects.* J Biol Chem, 2004. **279**(41): p. 42826-35.

93. Merkle, D., et al., *Analysis of DNA-dependent protein kinase-mediated DNA end joining by two-photon fluorescence cross-correlation spectroscopy.* Biochemistry, 2006. **45**(13): p. 4164-72.

94. Ma, Y. and M.R. Lieber, *DNA length-dependent cooperative interactions in the binding of Ku to DNA.* Biochemistry, 2001. **40**(32): p. 9638-46.

95. Weterings, E. and D.J. Chen, *DNA-dependent protein kinase in nonhomologous end joining: a lock with multiple keys?* J Cell Biol, 2007. **179**(2): p. 183-6.

96. Bekker-Jensen, S. and N. Mailand, *Assembly and function of DNA double-strand break repair foci in mammalian cells.* DNA Repair (Amst), 2010. **9**(12): p. 1219-28.

97. Wyman, C. and R. Kanaar, *DNA double-strand break repair: all's well that ends well.* Annu Rev Genet, 2006. **40**: p. 363-83.

98. Khanna, K.K. and S.P. Jackson, *DNA double-strand breaks: signaling, repair and the cancer connection.* Nat Genet, 2001. **27**(3): p. 247-54.

99. Christmann, M., et al., *Mechanisms of human DNA repair: an update.* Toxicology, 2003. **193**(1-2): p. 3-34.

100. Wyman, C., D. Ristic, and R. Kanaar, *Homologous recombination-mediated double-strand break repair.* DNA Repair (Amst), 2004. **3**(8-9): p. 827-33.

101. Elliott, B. and M. Jasin, *Double-strand breaks and translocations in cancer.* Cell Mol Life Sci, 2002. **59**(2): p. 373-85.

102. Allen, C., et al., *DNA-dependent protein kinase suppresses double-strand break-induced and spontaneous homologous recombination.* Proc Natl Acad Sci U S A, 2002. **99**(6): p. 3758-63.

103. Spagnolo, L., et al., *Three-dimensional structure of the human DNA-PKcs/Ku70/Ku80 complex assembled on DNA and its implications for DNA DSB repair.* Mol Cell, 2006. **22**(4): p. 511-9.

104. Lassmann, M., et al., *In vivo formation of gamma-H2AX and 53BP1 DNA repair foci in blood cells after radioiodine therapy of differentiated thyroid cancer.* J Nucl Med, 2010. **51**(8): p. 1318-25.

105. Essers, J., A.B. Houtsmuller, and R. Kanaar, *Analysis of DNA recombination and repair proteins in living cells by photobleaching microscopy.* Methods Enzymol, 2006. **408**: p. 463-85.

106. Roche, Y., et al., *Fluorescence correlation spectroscopy of the binding of nucleotide excision repair protein XPC-hHr23B with DNA substrates.* J Fluoresc, 2008. **18**(5): p. 987-95.

107. Michelman-Ribeiro, A., et al., *Direct measurement of association and dissociation rates of DNA binding in live cells by fluorescence correlation spectroscopy.* Biophys J, 2009. **97**(1): p. 337-46.

108. Zeiss, C., *Applications Manual for ConfoCor 3.* 2006(B40-0015 e).

109. Bacia, K. and P. Schwille, *Practical guidelines for dual-color fluorescence cross-correlation spectroscopy.* Nat Protoc, 2007. **2**(11): p. 2842-56.

110. Kim, S.A., K.G. Heinze, and P. Schwille, *Fluorescence correlation spectroscopy in living cells.* Nat Methods, 2007. **4**(11): p. 963-73.

111. Rossow, M.J., et al., *Raster image correlation spectroscopy in live cells.* Nature Protocols, 2010. **5**(11): p. 1761-1774.

112. Wei, Z., et al., *Detecting DNA repair capacity of peripheral lymphocytes from cancer patients with UVC challenge test and bleomycin challenge test.* Mutagenesis, 2005. **20**(4): p. 271-277.

113. Benitez-Bribiesca, L. and P. Sanchez-Suarez, *Oxidative damage, bleomycin, and gamma radiation induce different types of DNA strand breaks in normal lymphocytes and thymocytes - A comet assay study.* Mechanisms of Cell Death, 1999. **887**: p. 133-149.

114. Grigaravicius, P., A. Rapp, and K.O. Greulich, *A direct view by immunofluorescent comet assay (IFCA) of DNA damage induced by nicking and cutting enzymes, ionizing (137)Cs radiation, UV-A laser microbeam irradiation and the radiomimetic drug bleomycin.* Mutagenesis, 2009. **24**(2): p. 191-7.

BIOGRAPHICAL INFORMATION

Salim Abdallah Salim Abdisalaam was born in Pangani, Tanga, Tanzania. He obtained his undergraduate degree in Chemical and Process Engineering at the University of Dar es Salaam. He did his master degree in Computer Science with minor in Software Engineering at Texas State University. He then pursued his PhD in Bioengineering at joint program between University of Texas at Arlington and University of Texas Southwestern Medical Center at Dallas. His research interests include using confocal scanning correlation spectroscopy imaging techniques to study DNA repair proteins kinetics in living cells before and after γ-irradiation and radiomimetic chemicals. He uses different fluorescence fluctuations techniques including fluorescence correlation spectroscopy (FCS), Raster-scan Image correlation spectroscopy (RICS), Number and Brightness (N&B) analysis and strip-FRAP to study kinetics and dynamics of these proteins in living cells. Due to photobleaching effects and limitation of quantifying kinetics for longer period of time, he is extending his research by using two-photon microscopy together with femtosecond pulse shaping technique to probe these fluorescent proteins.